nature metabolism

ARTICLES

https://doi.org/10.1038/s42255-018-0005-8

Transferrin receptor 2 controls bone mass and pathological bone formation via BMP and Wnt signalling

Martina Rauner[1,2,17*], Ulrike Baschant[1,2,17], Antonella Roetto[3], Rosa Maria Pellegrino[3], Sandra Rother[4], Juliane Salbach-Hirsch[1,2], Heike Weidner[1,2], Vera Hintze[4], Graeme Campbell[5], Andreas Petzold[6], Regis Lemaitre[7], Ian Henry[8], Teresita Bellido[9], Igor Theurl[10], Sandro Altamura[11], Silvia Colucci[11], Martina U. Muckenthaler[11], Georg Schett[12], Davide S. K. Komla-Ebri[13], J. H. Duncan Bassett[13], Graham R. Williams[13], Uwe Platzbecker[2,14,15] and Lorenz C. Hofbauer[1,2,15,16]

Transferrin receptor 2 (Tfr2) is mainly expressed in the liver and controls iron homeostasis. Here, we identify Tfr2 as a regulator of bone homeostasis that inhibits bone formation. Mice lacking Tfr2 display increased bone mass and mineralization independent of iron homeostasis and hepatic Tfr2. Bone marrow transplantation experiments and studies of cell-specific Tfr2-knockout mice demonstrate that Tfr2 impairs BMP-p38MAPK signalling and decreases expression of the Wnt inhibitor sclerostin, specifically in osteoblasts. Reactivation of MAPK or overexpression of sclerostin rescues skeletal abnormalities in Tfr2-knockout mice. We further show that the extracellular domain of Tfr2 binds bone morphogenic proteins (BMPs) and inhibits BMP-2-induced heterotopic ossification by acting as a decoy receptor. These data indicate that Tfr2 limits bone formation by modulating BMP signalling, possibly through direct interaction with BMP either as a receptor or as a co-receptor in complex with other BMP receptors. Finally, the Tfr2 extracellular domain may be effective in the treatment of conditions associated with pathological bone formation.

Iron is indispensable for red blood cell production, bacterial defence, and cellular respiration[1]; however, iron excess is cytotoxic. Therefore, systemic iron levels are maintained in a narrow range to avoid iron deficiency and anaemia or iron overload that leads to multiorgan damage. Compared with other organs, bone is highly susceptible to changes in iron homeostasis. Bone mineral density is negatively associated with systemic iron concentrations[2], and patients suffering from hereditary haemochromatosis, a disorder characterized by iron overload, develop premature osteoporosis[3]. Despite these observations, the relationship between iron homeostasis and bone turnover remains largely unexplored.

Systemic iron concentrations are maintained by balancing dietary iron absorption and iron recycling from the reticuloendothelial system[1]. Hepcidin is a hepatic peptide hormone and key regulator of iron homeostasis[4]. By binding to ferroportin, an iron exporter, hepcidin causes the internalization and degradation of ferroportin, thereby limiting iron export in circulation. Dysregulation of this mechanism leads to iron overload. Accordingly, mutations in the gene encoding hepcidin or hepcidin-regulating genes cause hereditary haemochromatosis[5].

Tfr2 is a key regulator of hepcidin. Similar to humans, mice with global or liver-specific deletion of *Tfr2* accumulate iron in the liver[6–9]. Tfr2 is proposed to control iron homeostasis by regulating hepcidin expression and has two isoforms: Tfr2α, which represents the full-length protein and regulates iron homeostasis in the liver; and Tfr2β, which lacks the intracellular and transmembrane domains and plays an important role in iron efflux in the spleen[8]. To date, the mechanisms by which Tfr2 senses and regulates systemic iron concentrations remain incompletely understood. However, holotransferrin (holo-Tf) can bind Tfr2 and prolong its half-life[10]. Thus, Tfr2 has been postulated to sense circulating iron and activate hepcidin in response to elevated transferrin saturation.

Tfr2-deficient hepatocytes have reduced BMP and p38MAPK/ERK signaling[11–13], implicating these pathways in its signal transduction. Although BMP signalling is mostly known for its critical role in bone development and postnatal bone homeostasis[14], it has also emerged as an important regulator of iron homeostasis. Deficiency

[1]Department of Medicine III, Technische Universität Dresden, Dresden, Germany. [2]Center for Healthy Aging, Technische Universität Dresden, Dresden, Germany. [3]Department of Clinical and Biological Science, University of Torino, Torino, Italy. [4]Institute of Materials Science, Max Bergmann Center of Biomaterials, Technische Universität Dresden, Dresden, Germany. [5]Institute of Biomechanics, Hamburg University of Technology, Hamburg, Germany. [6]Deep Sequencing, Biotechnology Center, Technische Universität Dresden, Dresden, Germany. [7]Max Planck Institute for Cell Biology and Genetics, Protein Unit, Dresden, Germany. [8]Max Planck Institute for Cell Biology and Genetics, Scientific Computing Facility, Dresden, Germany. [9]Department of Anatomy and Cell Biology and Department of Medicine, Division of Endocrinology, School of Medicine, Indiana University, Indianapolis, IN, USA. [10]Department of Internal Medicine VI, Medical, University of Innsbruck, Innsbruck, Austria. [11]Department of Pediatric Hematology, Oncology and Immunology, University of Heidelberg, Heidelberg, Germany. [12]Department of Internal Medicine 3, Friedrich-Alexander-University Erlangen-Nuremberg (FAU) and University Hospital Erlangen, Erlangen, Germany. [13]Molecular Endocrinology Laboratory, Department of Medicine, Imperial College London, London, United Kingdom. [14]Department of Medicine II, University Clinic, Leipzig, Germany. [15]German Cancer Consortium (DKTK) Partner Site Dresden, Dresden, Germany. [16]Center for Regenerative Therapies Dresden, Technische Universität Dresden, Dresden, Germany. [17]These authors contributed equally: M. Rauner, U. Baschant. *e-mail: martina.rauner@ukdd.de

of several components of the BMP pathway (*Bmpr1a*, *Bmpr2*, *Acvr1*, *Acvr2a*, *Smad4*, *Bmp2*, *Bmp6*) or their pharmacological inhibition results in iron overload[15–20]. Moreover, hemojuvelin, another regulator of hepcidin expression, has been identified as a hepatic BMP co-receptor[16], further linking BMP signalling to iron homeostasis. Importantly, activating mutations in one of the BMP receptors that controls iron homeostasis, *ACVR1*, cause a rare disorder in humans, fibrodysplasia ossificans progressiva (FOP), which is characterized by excessive heterotopic ossification[21]. Thus, balancing BMP signalling is necessary to maintain bone and iron homeostasis in a physiological range.

Recent evidence indicates that Tfr2 is not restricted to the liver, but is also expressed in erythroid progenitors to ensure their proper differentiation[8,22,23]. As BMP signalling has a critical role in the skeleton[14,24], we hypothesized that Tfr2 may possess additional extrahepatic functions and regulate bone homeostasis. Here, we demonstrate that Tfr2 is a novel negative regulator of bone turnover. By binding BMP ligands, Tfr2 activates p38MAPK signalling in osteoblasts to induce expression of the Wnt inhibitor sclerostin and limit bone formation. Finally, by taking advantage of the BMP-binding property of the Tfr2 extracellular domain, we show that this protein fragment effectively inhibits heterotopic ossification in two preclinical models, suggesting that it may also be efficacious in treating disorders of pathological bone formation.

Results

***Tfr2* deficiency leads to high bone mass.** To investigate whether the iron-sensing receptor Tfr2 regulates bone homeostasis, we studied *Tfr2*$^{-/-}$ mice, which are iron overloaded. Consistent with previous reports[8,25], transferrin saturation, serum iron and ferritin concentrations, and iron content in the liver were increased in *Tfr2*$^{-/-}$ mice compared with wild-type (WT) mice (Supplementary Fig. 1a–d). Additionally, atomic absorptiometry revealed a higher iron content in the cortical bone of *Tfr2*$^{-/-}$ mice (Supplementary Fig. 1e). As iron overload is associated with bone loss[3], we expected a decrease in bone volume in *Tfr2*$^{-/-}$ mice. However, in contrast to the low bone mass phenotype of mice with diet-induced iron overload, and in different mouse models of haemochromatosis, including *Hfe*$^{-/-}$ mice[26] and *Fpn*^{C326S} mutant mice[27] (Supplementary Fig. 2a–c), *Tfr2*$^{-/-}$ mice displayed a 1.5- to 3-fold increase in trabecular bone volume in the femur and vertebrae and a 1.5-fold increase in cortical bone density compared with WT controls (Fig. 1a,b). High bone mass was independent of sex and declined with age (Supplementary Fig. 3a,b). At a structural level, *Tfr2*$^{-/-}$ vertebrae had increased trabecular number (Tb.N) and thickness (Tb.Th) and decreased separation (Tb.Sp) (Fig. 1c–e). Furthermore, *Tfr2*$^{-/-}$ mice had increased trabecular bone micromineralization density (Supplementary Fig. 3c), which, together with the increased bone volume, enhances bone strength (Fig. 1f).

We performed dynamic and static histomorphometry to determine whether the high bone mass phenotype was a consequence of increased bone formation or decreased bone resorption. *Tfr2* deficiency resulted in an increase in both osteoblast and osteoclast parameters. The bone formation rate and the serum concentration of the bone formation marker pro-collagen type I N-terminal peptide (P1NP) were elevated more than two-fold in *Tfr2*$^{-/-}$ mice, and the number of osteoclasts and the serum concentration of the bone resorption marker C-terminal telopeptide of type I collagen (CTX) were similarly increased (Fig. 1g–l). The high bone turnover was present in both male and female mice, at all ages studied (Supplementary Fig. 3d,e). Interestingly, *Tfr2*$^{-/-}$ mice were not protected from ovariectomy-induced bone loss, but lost even more bone than WT mice (Fig. 1m). Taken together, these data demonstrate that Tfr2 controls not only iron homeostasis, but also bone turnover.

High bone mass in *Tfr2*-deficient mice is independent of hepatic iron status or *Tfr2* expression in the liver. As *Tfr2*$^{-/-}$ mice are iron overloaded and have high bone mass (though iron overload is commonly associated with decreased bone mass[3,28]), we investigated whether abnormal iron metabolism contributes to the skeletal phenotype in *Tfr2*$^{-/-}$ mice. Thus, *Tfr2*$^{-/-}$ mice were given an iron-free diet for 8 weeks from weaning or were treated with the iron chelator deferoxamine for 3 weeks from 10 weeks of age. Despite successful iron depletion by both regimens, bone mass remained elevated in *Tfr2*$^{-/-}$ mice (Fig. 2a–d), thus indicating that the high bone mass phenotype in *Tfr2*$^{-/-}$ mice is independent of the hepatic iron status.

To corroborate these findings, we studied two distinct *Tfr2*-mutant mouse models, which globally lack *Tfr2β* but have contrasting *Tfr2α* expression that results in divergent abnormalities of iron homeostasis[8]: *Tfr2* knock-in (KI) mice, which globally lack *Tfr2β* but have normal *Tfr2α* and, thus, normal iron parameters; and hepatocyte-specific *Tfr2* knock-out (LCKO) mice, which globally lack *Tfr2β* and have *Tfr2α* deficiency that is restricted to the liver, but are severely iron overloaded. Both mutant mouse models showed comparable bone volume fractions compared with controls (Fig. 2e,f), thus indicating that neither *Tfr2β* nor hepatic *Tfr2α* play a role in the control of bone homeostasis.

***Tfr2* deficiency in osteoblasts drives the high bone mass phenotype.** To explore whether Tfr2 regulates bone mass directly via its expression in skeletal cells, we determined the expression pattern of *Tfr2α* and *Tfr2β* in various mouse tissues. As expected, *Tfr2α* was predominantly expressed in the liver, followed by expression in femoral cortical bone (Supplementary Fig. 4a). *Tfr2β* mRNA expression was also detected in femoral cortical bone, but at a much lower level (C_T (threshold cycle) value, spleen (positive control): 26; C_T value, bone: 32). Using an antibody that binds to the extracellular domain of Tfr2, and thus detects both Tfr2α and Tfr2β isoforms, we confirmed expression of Tfr2 in vertebral bone sections, showing Tfr2-positive osteoclasts, osteoblasts, and osteocytes (Fig. 3a,d). Staining of bone sections from *Tfr2*$^{-/-}$ mice showed no nonspecific binding of the Tfr2 antibody (Supplementary Fig. 3b). Osteoclasts and osteoblasts differentiated from bone marrow of WT mice both expressed *Tfr2α* and *Tfr2β* mRNA transcripts ex vivo, but expression of *Tfr2β* was very low in each cell type (data for *Tfr2β* not shown). *Tfr2α* was readily detectable in osteoclasts and osteoblasts, with peak levels of expression in mature osteoclasts (day 7 of 7) and in immature osteoblasts (day 7 of 21) (Fig. 3b,e). Immunocytochemistry confirmed Tfr2 expression in osteoclasts and osterix-expressing osteoblasts that were differentiated ex vivo (Fig. 3c,f). Subcellular fractioning of osteoblasts further localized the majority of Tfr2 to the membrane fraction (Fig. 3g). A low signal was also detected in the cytoplasm.

To determine if Tfr2 in osteoclasts or in osteoblasts regulates bone turnover, we performed reciprocal bone marrow transplantations. In WT and *Tfr2*$^{-/-}$ mice, bone marrow transplantation had no effect on vertebral or femoral bone volume irrespective of donor genotype (Fig. 3h), suggesting that Tfr2 deficiency in the haematopoietic compartment is not responsible for the high bone mass phenotype in *Tfr2*$^{-/-}$ mice. Consistent with these findings, specific deletion of *Tfr2* in the myeloid lineage (*Lysm-cre*) and in mature osteoclasts (*Ctsk-cre*) did not affect bone volume at the spine (Fig. 3i). Femoral bone volume decreased in *Tfr2*$^{f/f}$*;Lysm-cre* mice, but not in *Tfr2*$^{f/f}$*;Ctsk-cre* mice (Supplementary Fig. 5a). By contrast, deletion of *Tfr2* in osteoblast progenitors, in which *Tfr2* expression is highest, increased bone mass at the femur and spine (Fig. 3j), increased trabecular number, and decreased trabecular separation (Fig. 3k). Bone formation was increased in *Tfr2*$^{f/f}$*;Osx-cre* mice (*Tfr2* deletion in osteoblast precursors), as reflected by higher serum P1NP levels (Fig. 3l) and a higher bone formation rate (Fig. 3m). Finally, deletion of *Tfr2* in osteoblasts did not change osteoclast numbers, but tended to increase serum levels of CTX (Fig. 3n,o).

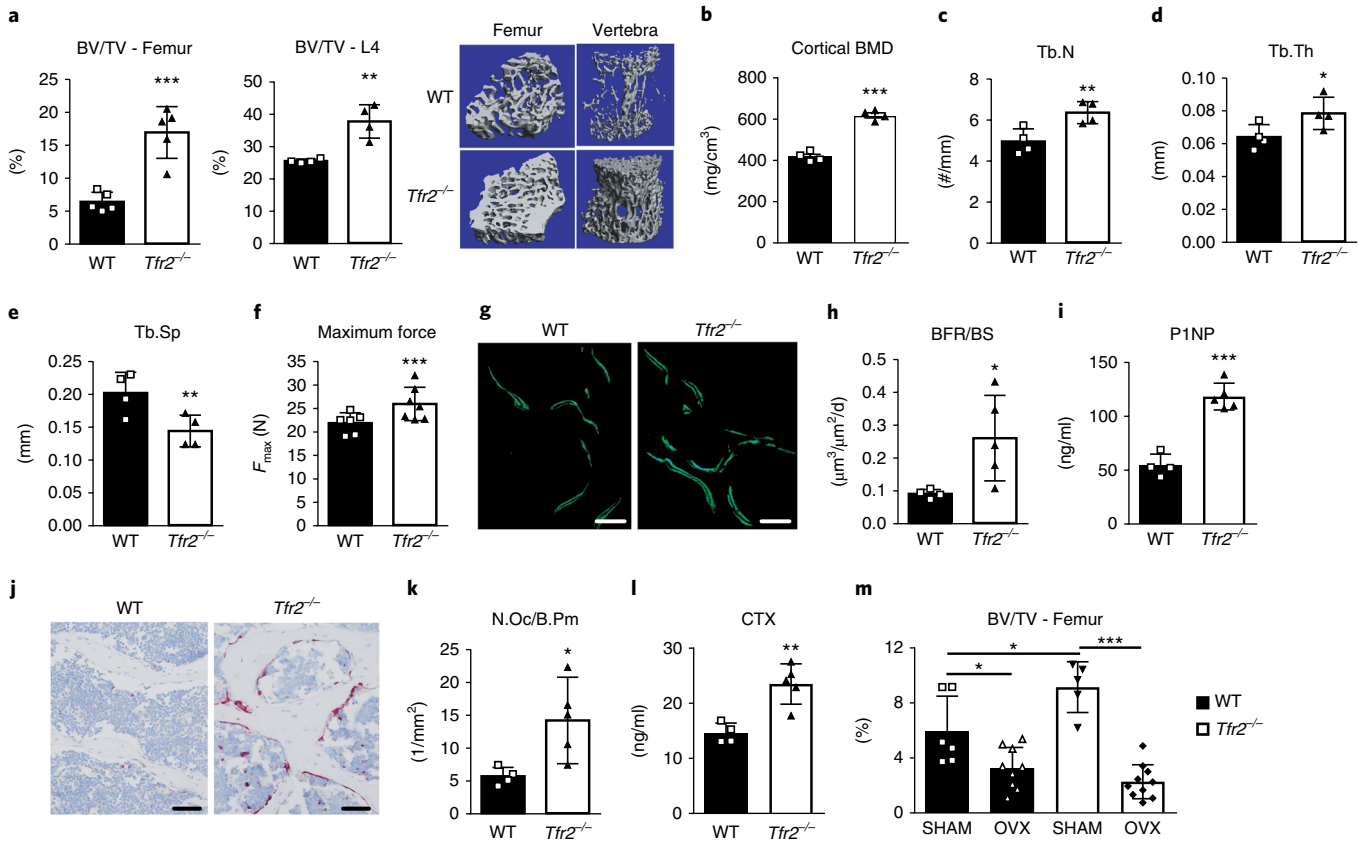

Fig. 1 | *Tfr2* deficiency results in high bone mass. a–l, The bones and serum bone turnover markers of 10-week-old male WT or *Tfr2*$^{-/-}$ mice were analysed using µCT, histology, and ELISAs. **a**, Three-dimensional reconstruction and quantitation of the bone volume per total volume (BV/TV) of the distal femur and the fourth vertebral body of WT and *Tfr2*$^{-/-}$ mice. Femur, $n=5$ mice per group; vertebral body, $n=4$ mice per group. **b**, Cortical bone mineral density (BMD) at the femoral midshaft. $n=4$ mice per group. **c–e**, Quantitation of vertebral trabecular number (Tb.N) (**c**), trabecular thickness (Tb.Th) (**d**), and trabecular separation (Tb.Sp) (**e**). $n=4$ mice per group. **f**, Maximum force at the femoral shaft assessed by three-point-bending. (WT, $n=6$; *Tfr2*$^{-/-}$, $n=7$). **g**, Representative histological sections from the third vertebral body of WT and *Tfr2*$^{-/-}$ mice showing calcein double staining (green). Scale bar, 100 µm. These experiments were repeated four times with similar results. **h**, Quantification of the bone formation rate per bone surface (BFR/BS). WT, $n=4$; *Tfr2*$^{-/-}$, $n=6$. **i**, Quantification of serum P1NP as a marker of bone formation. WT, $n=4$; *Tfr2*$^{-/-}$, $n=5$. **j**, Representative histological tartrate-resistant acid phosphatase sections from the fourth vertebral body of WT and *Tfr2*$^{-/-}$ mice showing osteoclasts stained in pink. Scale bar, 100 µm. These examinations were performed four times with similar results. **k**, Quantification of the number of osteoclasts per bone perimeter (N.Oc/B.Pm). WT, $n=4$; *Tfr2*$^{-/-}$, $n=6$. **l**, Quantification of serum CTX as a marker of bone resorption. WT, $n=4$; *Tfr2*$^{-/-}$, $n=5$. **a–f**, **h**,**i**,**k**,**l**, A two-tailed *t* test was used for statistical analysis. **m**, µCT analysis of femoral bone of 12-week-old sham-operated (SHAM) or ovariectomized (OVX) WT and *Tfr2*$^{-/-}$ mice. WT SHAM, $n=6$; WT OVX, $n=9$; *Tfr2*$^{-/-}$ SHAM, $n=5$; *Tfr2*$^{-/-}$ OVX, $n=10$. Two-way ANOVA with Bonferroni post hoc test was used for statistical analysis. Data in all subpanels are presented as mean ± s.d. $^{*}P<0.05$, $^{**}P<0.01$, $^{***}P<0.001$.

Consistent with data published from *Tfr2*$^{f/f}$;*Lysm-cre* mice[29], *Tfr2*$^{f/f}$;*Ctsk-cre* and *Tfr2*$^{f/f}$;*Osx-cre* mice showed a normal liver iron content (Supplementary Fig. 5b,c). Taken together, these data indicate that Tfr2 predominantly in osteoblasts regulates bone formation but does not contribute to systemic iron homeostasis.

***Tfr2* deficiency in osteoblasts attenuates BMP-MAPK signalling and results in decreased expression of Wnt inhibitors.** Because data indicated a direct role for Tfr2 in osteoblasts, we performed a genome-wide RNA sequencing analysis using primary osteoblasts from WT and *Tfr2*$^{-/-}$ mice to identify signalling pathways affected by deletion of *Tfr2*. A total of 5,841 differentially expressed genes were identified (Supplementary Data Set 1). We performed gene ontology analysis to determine the biological processes affected by *Tfr2* deficiency (complete list in Supplementary Table 1). Genes upregulated in *Tfr2*$^{-/-}$ osteoblasts were involved in negative regulation of protein secretion and muscle systems. By contrast, genes involved in ossification, extracellular matrix organization, negative regulation of Wnt signalling, and Smad phosphorylation were downregulated in *Tfr2*$^{-/-}$ osteoblasts (Supplementary Fig. 6a). These data are consistent with those of molecular function and cellular component analyses, which revealed under-representation of genes involved in glycosaminoglycan and heparin binding, as well as BMP receptor binding and proteinaceous extracellular matrix and collagen formation (Supplementary Fig. 6a). Gene set enrichment analysis further demonstrated under-representation of genes involved in late osteoblastic differentiation and Wnt signalling, the latter of which is associated with marked suppression of the Wnt inhibitor Dickkopf-1 (*Dkk1*) (Supplementary Fig. 6b,c; complete list of significantly enriched gene sets is in Supplementary Table 2).

Dkk1 and *Sost* (encoding the Wnt inhibitor sclerostin) were among the 25 most downregulated genes in *Tfr2*$^{-/-}$ osteoblasts ex vivo (Fig. 4a). Reduced expression of the two Wnt inhibitors was verified via quantitative PCR (qPCR) and is consistent with increased expression of the Wnt target genes *Axin2*, *Lef1*, and *Cd44* (Supplementary Fig. 6c). *Dkk1* and *Sost* mRNA levels were also downregulated in osteoblasts obtained from *Tfr2*$^{f/f}$;*Osx-cre* mice (Fig. 4b). Furthermore, expression of the osteocyte-associated genes

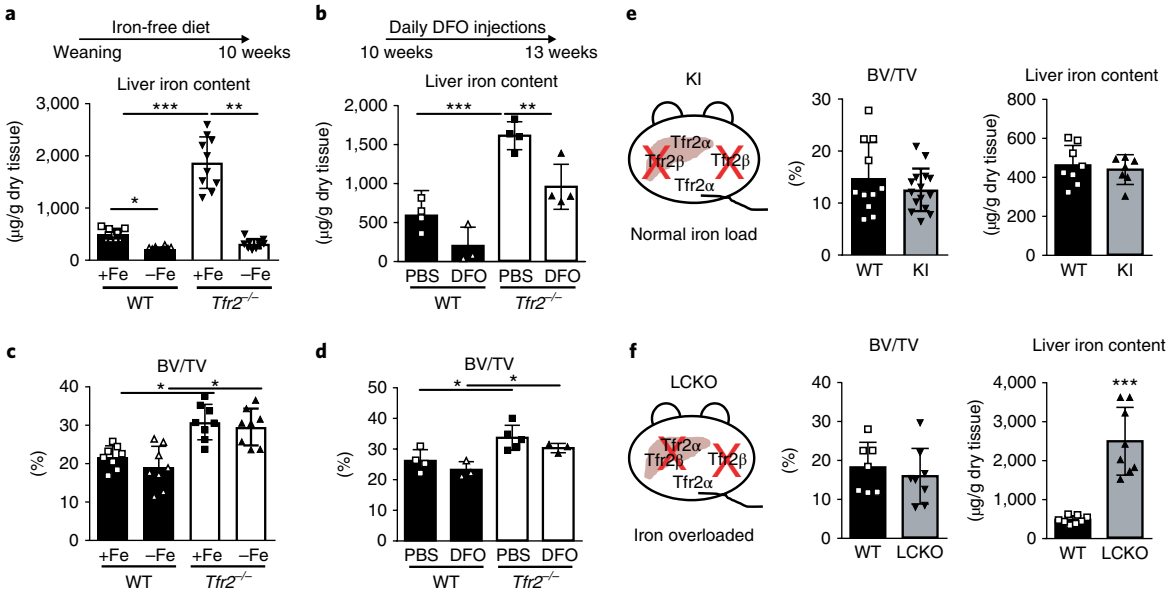

Fig. 2 | High bone mass in *Tfr2*$^{-/-}$ mice is independent of iron overload and the hepatic function of Tfr2. a,**c**, Male WT and *Tfr2*$^{-/-}$ mice received a purified diet without iron (-Fe) starting from weaning until the age of 10 weeks. Control mice received a standard diet with 0.2 g iron/kg food (+Fe). **a**, Liver iron content was determined on dried tissue using photometry (mean ± s.d.; $n = 10$ mice per group). **c**, Bone volume/total volume (BV/TV) was assessed using µCT (mean ± s.d.; WT +Fe, $n = 9$; WT -Fe, *Tfr2*$^{-/-}$ +Fe, and *Tfr2*$^{-/-}$ -Fe, $n = 8$ per group). **b**,**d**, 10-week-old female WT and *Tfr2*$^{-/-}$ mice received daily intraperitoneal injections of 250 mg/kg deferoxamine (DFO) or PBS for 3 weeks. At 13 weeks of age, mice were euthanized to measure liver iron content (**b**) and BV/TV (**d**). (mean ± s.d.; WT +Fe, $n = 4$; WT -Fe, $n = 3$; *Tfr2*$^{-/-}$ +Fe, $n = 4$, *Tfr2*$^{-/-}$ -Fe, $n = 4$). **a**–**d**, Two-way ANOVA with Bonferroni post hoc test was used for statistical analysis. **e**, Schematic representation of *Tfr2*-KI mice, which lack the *Tfr2β* isoform and BV/TV and liver iron content of 10-week-old male *Tfr2*-KI mice and control mice (BV/TV, WT $n = 11$, KI $n = 15$; liver iron, WT $n = 8$, KI $n = 7$). **f**, Schematic representation of the Tfr2 setup of LCKO mice on a *Tfr2*-KI background and BV/TV and liver iron content of 10-week-old male LCKO and WT mice ($n = 8$ per group). **e**,**f**, A two-tailed *t* test was used for statistical analysis. All data are presented as mean ± s.d. $^{*}P < 0.05$, $^{**}P < 0.01$, $^{***}P < 0.001$.

Phex and *Dmp1* decreased (Supplementary Fig. 6c). Importantly, impaired expression of osteocytic markers was not caused by reduced osteocyte number in *Tfr2*$^{-/-}$ bone (WT, 8.73 ± 2.74 versus *Tfr2*$^{-/-}$, 9.77 ± 0.85 osteocytes per bone volume fraction). Low concentrations of sclerostin and Dkk1 were detected in the serum of *Tfr2*$^{-/-}$ mice (Fig. 4c), along with a greater proportion of osteoblasts and osteocytes with high expression of β-catenin and axin-2 (Fig. 4d). Finally, western blot analysis of β-catenin showed increased Wnt signalling in *Tfr2*$^{-/-}$ osteoblasts differentiated for 7 d (Fig. 4e).

Results from deep-sequencing analysis suggested decreased BMP signalling in *Tfr2*$^{-/-}$ osteoblasts, and recent studies have indicated that *Sost* and *Dkk1* are downstream targets of BMP signalling[30,31]. Thus, we analysed BMP target genes as well as the basal canonical (Smad) and non-canonical (MAPK) BMP signalling pathways in *Tfr2*$^{-/-}$ and WT osteoblasts. *Smad6* and *Id1* were significantly downregulated in *Tfr2*$^{-/-}$ osteoblasts, whereas *Id2* expression was similar between WT and *Tfr2*$^{-/-}$ osteoblasts (Supplementary Fig. 6c). Smad1, Smad5, and Smad8 phosphorylation as well as ERK and p38 activation were decreased in *Tfr2*$^{-/-}$ osteoblasts compared with WT osteoblasts (Fig. 4e). Moreover, activation of BMP signalling after BMP-2 treatment demonstrated that Smad activation was delayed in *Tfr2*$^{-/-}$ osteoblasts, whereas activation of p38MAPK and ERK was persistently impaired (Fig. 4f,g). The reduced activation of noncanonical BMP signalling in *Tfr2*$^{-/-}$ osteoblasts was not restricted to

Fig. 3 | Deficiency of *Tfr2* in osteogenic cells increases bone mass. a,**d**, Immunohistochemical analysis of Tfr2 on vertebral bone of WT mice. One representative image is shown out of three experiments. Arrows indicate Tfr2 expression in multinucleated osteoclasts and osteoblasts/osteocytes (osteoblasts, black arrows; osteocytes, orange arrows). Scale bar, 20 µm. **b**,**e**, *Tfr2α* mRNA expression during osteoclast (**b**) and osteoblast (**e**) differentiation of WT cells ($n = 4$). **c**,**f**, Immunofluorescence staining for Tfr2 in mature osteoclasts (**c**) and immature osteoblasts (**f**). Scale bar, 20 µm. This staining was repeated twice with similar results. **g**, Subcellular fractioning of day 7 osteoblast protein lysates from WT mice. One representative blot is shown out of three experiments. CP, cytoplasm; M, membrane; Nuc, nuclear fraction; Cx-43, connexin-43. **h**, Bone marrow was transplanted from 12-week-old male WT or *Tfr2*$^{-/-}$ mice (donor) into lethally irradiated 9-week-old male WT and *Tfr2*$^{-/-}$ recipient (recip) mice. After 16 weeks, the BV/TV was measured using µCT (L4: WT-WT, $n = 11$; *Tfr2*$^{-/-}$-WT, $n = 11$; *Tfr2*$^{-/-}$-*Tfr2*$^{-/-}$, $n = 7$; WT-*Tfr2*$^{-/-}$, $n = 9$; femur: WT-WT, $n = 12$; *Tfr2*$^{-/-}$-WT, $n = 10$; *Tfr2*$^{-/-}$-*Tfr2*$^{-/-}$, $n = 8$; WT-*Tfr2*$^{-/-}$, $n = 10$). Two-way ANOVA with Bonferroni post hoc test was used for statistical analysis. **i**, BV/TV of the fourth lumbar vertebrae of 10-week-old male *cre*-positive (Cre+) and *cre*-negative (Cre–) *Tfr2*$^{fl/fl}$;*Lysm-cre* and *Tfr2*$^{fl/fl}$;*Ctsk-cre* mice (*Tfr2*$^{fl/fl}$;*Lysm-cre*: Cre–, $n = 16$; Cre+, $n = 9$; *Tfr2*$^{fl/fl}$;*Ctsk-Cre*: Cre–, $n = 8$; Cre+, $n = 12$). **j**–**o**, Bone analysis of 10-week-old male cre-positive and cre-negative littermate control *Tfr2*$^{fl/fl}$;*Osx-Cre* mice. **j**, BV/TV (L4: Cre–, $n = 18$, Cre+, $n = 12$; femur: Cre–, $n = 18$, Cre+, $n = 13$). **k**, Trabecular number (Tb.N) and trabecular separation (Tb.Sp) (Tb.N., Cre– $n = 18$, Cre+, $n = 13$; Tb.Sp., Cre– $n = 19$, Cre+, $n = 12$). **l**, Serum levels of P1NP ($n = 6$ per group). **m**, Mineralizing surface per bone surface (MS/BS), mineral apposition rate (MAR), and bone formation rate per bone surface (BFR/BS) determined at the lumbar spine (MS/BS: Cre–, $n = 11$; Cre+, $n = 10$; MAR: Cre– $n = 9$, Cre+, $n = 6$; BFR: Cre– $n = 10$; Cre+, $n = 6$). **n**, Osteoclast surface per bone surface (Oc.S/BS) analysed at the lumbar spine (Cre–, $n = 7$, Cre+, $n = 6$). **o**, Serum CTX levels ($n = 6$ per group). **i**–**o**, A two-tailed Student's *t* test was used for statistical analysis. All data are presented as mean ± s.d. $^{*}P < 0.05$, $^{**}P < 0.01$, $^{***}P < 0.001$.

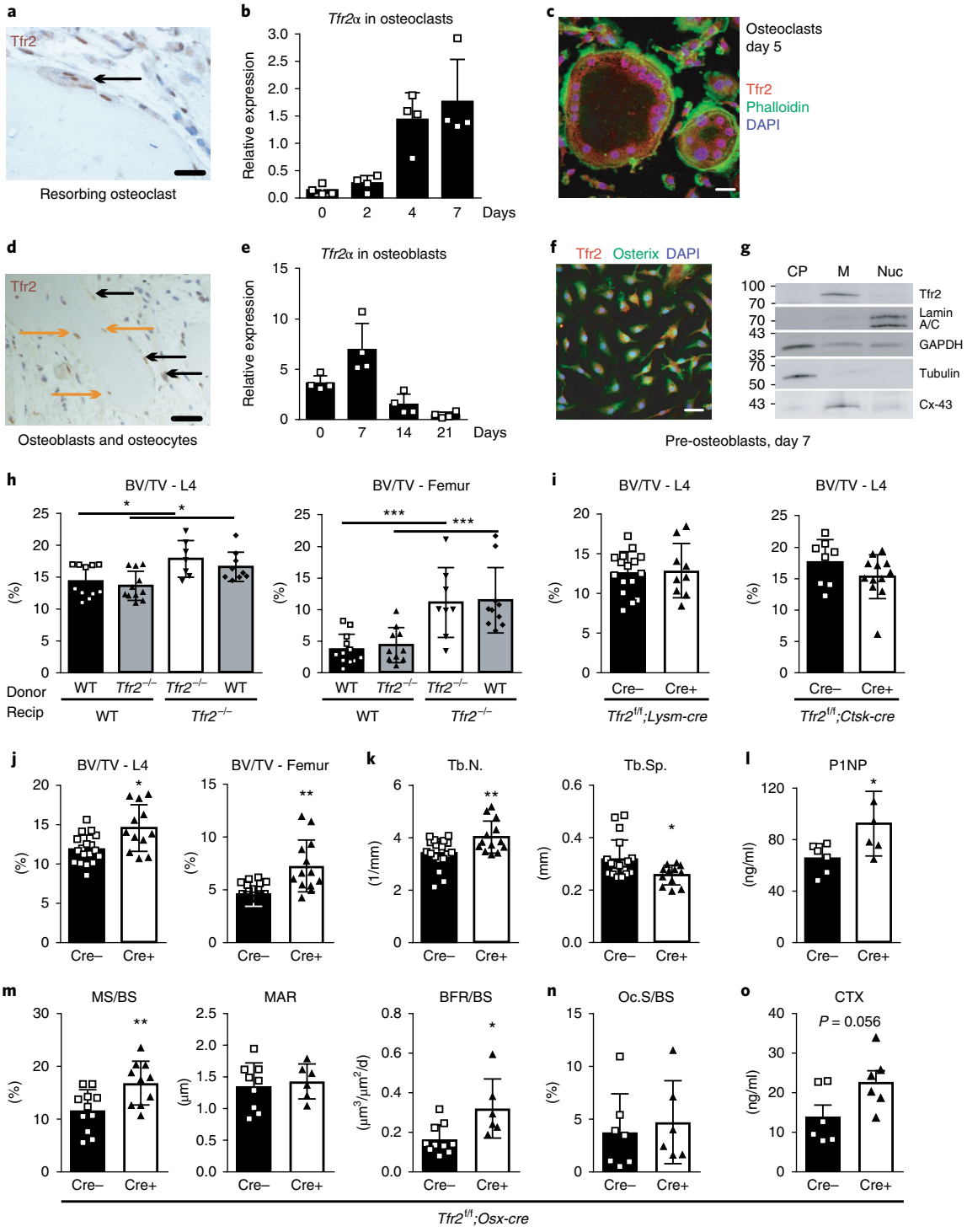

BMP-2 treatment, but was also observed after BMP-4 treatment and, to a lesser extent, BMP-6 stimulation (Fig. 4h and Supplementary Fig. 6d). Overall, *Tfr2* deficiency in osteoblasts results in impaired BMP signalling and increased activation of the Wnt pathway.

Reactivation of MAPK signalling or overexpression of sclerostin rescues high bone mass in *Tfr2* deficiency. We next investigated the mechanisms underlying the Tfr2-mediated regulation of *Sost* expression, as this may be a major driver of the Tfr2-dependent effects on bone. Using *Tfr2*$^{-/-}$ osteoblasts in vitro, we confirmed the lack of induction of *Sost* expression after stimulation with BMP-2, BMP-4, and BMP-7 (Fig. 5a). Conversely, overexpression of *Tfr2* in WT and *Tfr2*$^{-/-}$ osteoblasts markedly increased *Sost*, particularly after stimulation with BMP-2 (Fig. 5b and Supplementary Fig. 7a). To test the impact of sclerostin in producing the high bone mass phenotype in *Tfr2*$^{-/-}$ mice, we crossed *Tfr2*$^{-/-}$ mice with mice overexpressing human *SOST* in late osteoblasts and osteocytes (under the *Dmp1* 8-kb promoter). Overexpression of *SOST* significantly reduced the vertebral trabecular bone volume in *Tfr2*$^{-/-}$ mice (Fig. 5c) and normalized the bone formation rate (Fig. 5d). The osteoclast-covered bone surface was higher in *Tfr2*$^{-/-}$ mice and in WT mice overexpressing *SOST* in osteoblasts

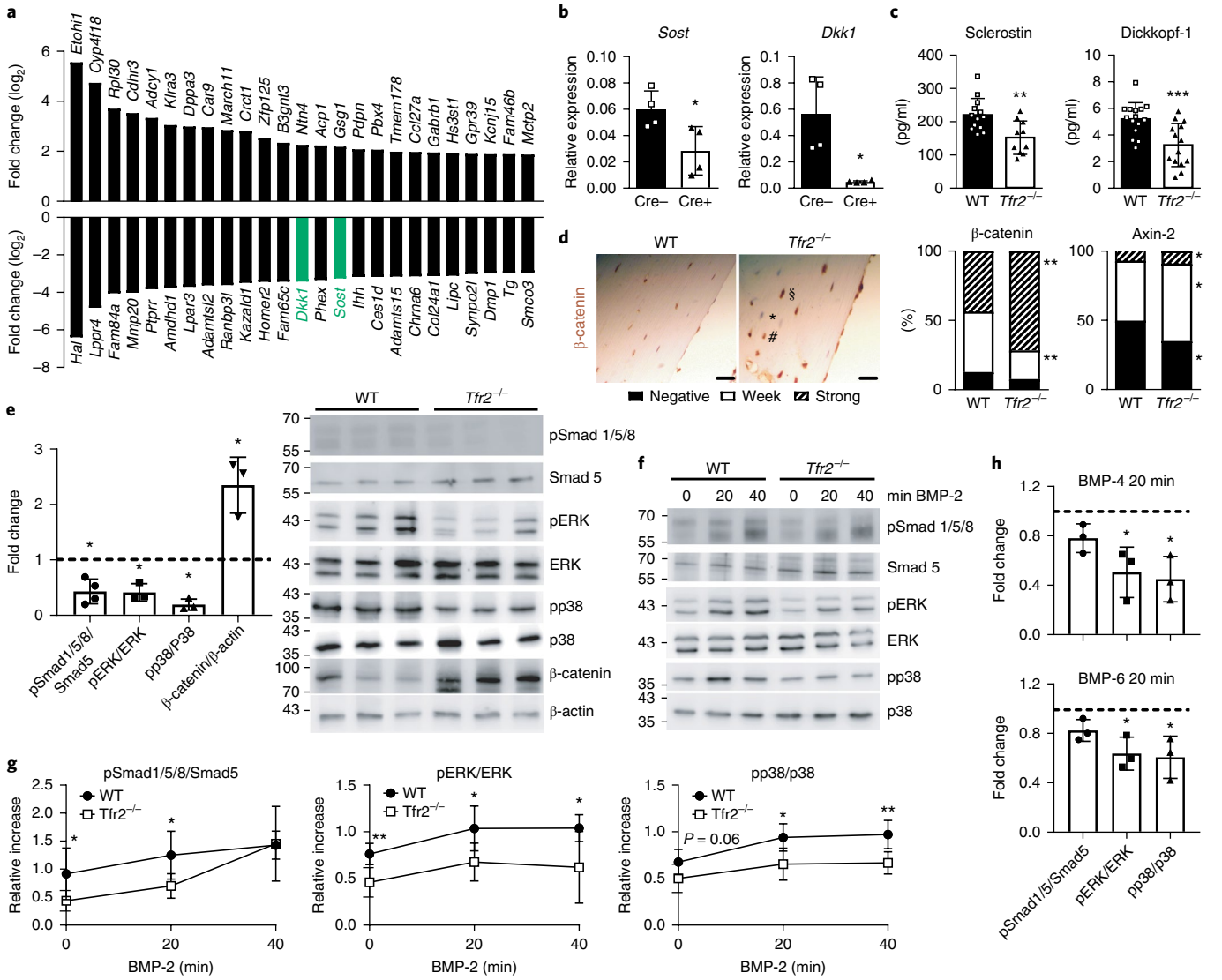

Fig. 4 | Downregulation of BMP signalling and Wnt inhibitors in *Tfr2* deficiency. a, Top 25 most increased and decreased genes identified using next-generation sequencing of day 7 osteoblasts from WT and *Tfr2*$^{-/-}$ mice ($n=4$ per genotype). **b**, Gene expression of *Dkk1* and *Sost* in day 7 differentiated osteoblasts from *Tfr2*$^{f/f}$;*Osx-cre* mice and littermate controls, normalized to β-actin ($n=4$ per group). **c**, Serum concentrations of Dickkopf-1 and sclerostin in WT and *Tfr2*$^{-/-}$ mice (sclerostin: WT, $n=13$; Tfr2$^{-/-}$, $n=10$; Dickkopf: WT, $n=15$; *Tfr2*$^{-/-}$, $n=14$). **d**, Immunohistochemical analysis of β-catenin and axin-2 on femoral bone sections from WT and *Tfr2*$^{-/-}$ mice. Scale bar, 20 µm. Cells were quantified according to their staining intensity (negative (*), weak (#), strong (§); $n=9$ per group). **e**, Analysis of the status of activated Smad and MAPK signalling in ex vivo–differentiated osteoblasts (day 7) from *Tfr2*$^{-/-}$ mice normalized to WT osteoblasts. Phosphorylated proteins were normalized to their unphosphorylated counterparts. Expression of β-catenin was normalized to β-actin. Quantification is the result of densitometry of five independent western blot experiments. Dotted line represents the WT level (Smad1/5/8, $n=4$; pERK, pp38, and β-catenin, $n=3$). **f**,**g**, Ex vivo–differentiated osteoblasts from WT and *Tfr2*$^{-/-}$ mice were treated with 50 ng/ml BMP-2 for 0, 20, and 40 min. After protein extraction, phosphorylation of signalling proteins was analysed using western blot (**f**). **g**, Graphs represent the quantification of four independent experiments ($n=4$ per group). **h**, Induction of Smad1/5, ERK, and p38 in WT and *Tfr2*$^{-/-}$ osteoblasts after 20 min of stimulation with 50 ng/ml BMP-4 or BMP-6. Dotted line represents the WT level. $n=3$ per group. **b**–**e**, **g**,**h**, A two-tailed *t* test was used for statistical analysis. All data are presented as mean ± s.d. (except **d**, which shows percentages). $^{*}P<0.05$, $^{**}P<0.01$, $^{***}P<0.001$.

and osteocytes compared with mice with normal *Sost* expression (Supplementary Fig. 7b).

Previous studies have indicated that BMPs stimulate *Sost* expression via the BMP-Smad and BMP-MAPK pathways[30,31]. Because pERK and pp38 were most markedly reduced in *Tfr2*$^{-/-}$ osteoblasts, and neither Smad1 nor Smad4 overexpression in *Tfr2*$^{-/-}$ osteoblasts restored *Sost* mRNA levels (Supplementary Fig. 7c–f), we reactivated the MAPK pathways using anisomycin to rescue *Sost* expression. Treatment with anisomycin induced ERK and p38 phosphorylation (Supplementary Fig. 7g) and increased *Sost* mRNA expression in *Tfr2*$^{-/-}$ and WT osteoblasts: 19-fold in *Tfr2*$^{-/-}$ osteoblasts and 14-fold in WT osteoblasts at 100 nM anisomycin (Fig. 5e). Similarly, treatment of *Tfr2*$^{-/-}$ mice with anisomycin for 3 weeks increased serum levels of sclerostin (Fig. 5f), reduced osteoblast numbers (Fig. 5g), and decreased bone volume back to WT levels (Fig. 5h). Osteoclast numbers were not altered by anisomycin treatment (Supplementary Fig. 7h). Finally, we investigated which specific MAPK pathway, ERK or p38, regulates *Sost* expression. Overexpression of *Mapk14* (encoding p38α), but not *Mapk1* (encoding ERK2), restored reduced *Sost* levels in *Tfr2*$^{-/-}$ osteoblasts (Fig. 5i,j). Thus, Tfr2 controls bone mass by inducing *Sost* expression via the p38MAPK signalling pathway.

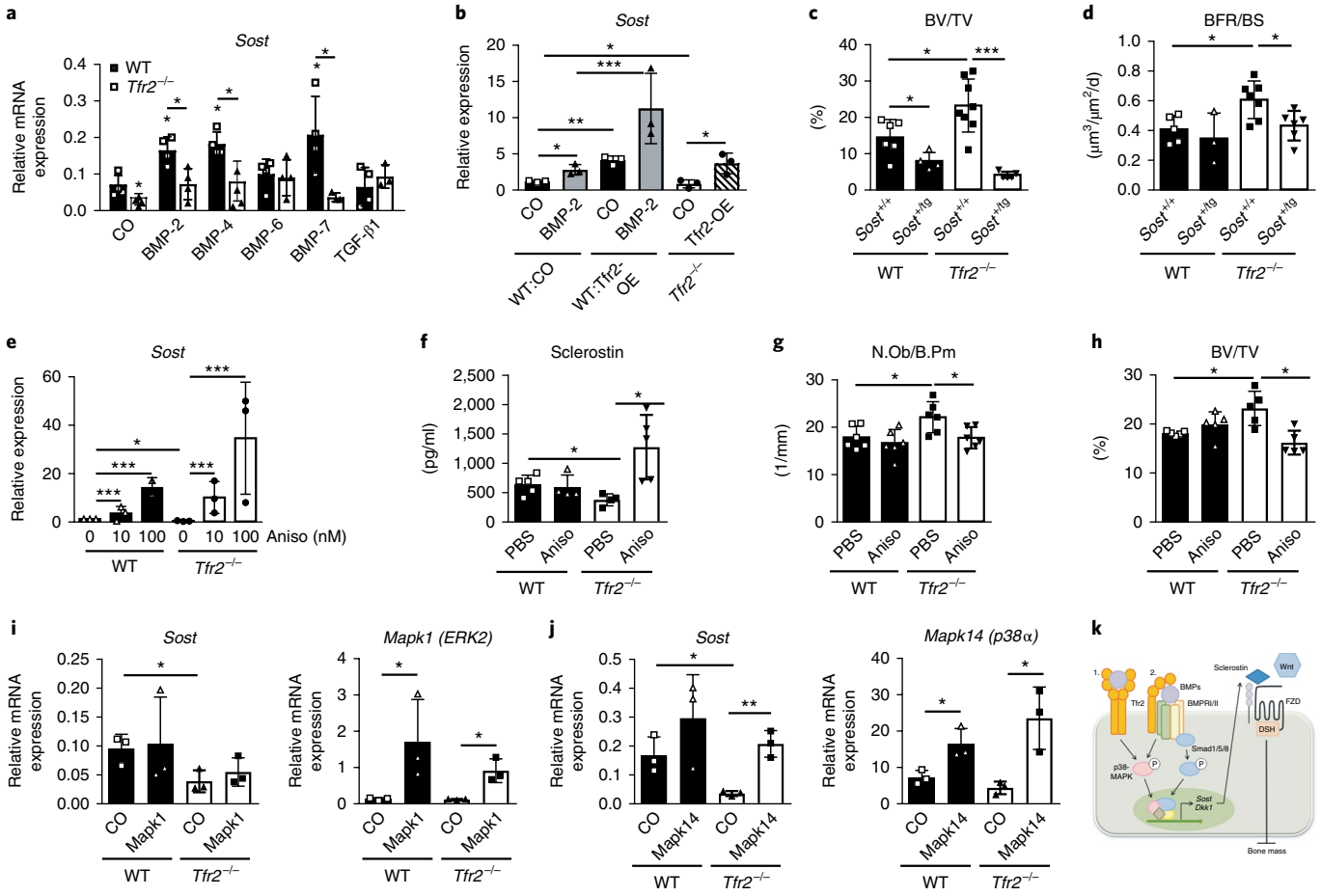

Fig. 5 | High bone mass in *Tfr2* deficiency is rescued by overexpressing *SOST* or reactivating MAPK signalling. a, WT or *Tfr2*$^{-/-}$ osteoblasts were differentiated for 7 d and stimulated with 50 ng/ml BMPs or TGF-β1 for 48 h. *Sost* mRNA expression was determined using qPCR ($n=4$). A two-tailed *t* test was used for statistical analysis. **b**, Day 7 WT or *Tfr2*$^{-/-}$ osteoblasts were transfected with an empty pcDNA3.1 vector (CO) or a pcDNA3.1 vector containing the Tfr2 gene (Tfr2-OE). Cells were treated with either 50 ng/ml BMP-2 or PBS. After 48 h, mRNA expression of *Sost* was determined using qPCR ($n=3$). **c**, Bone volume/total volume (BV/TV), WT/Sost$^{+/+}$ $n=6$, WT Sost$^{+/tg}$ $n=4$, *Tfr2*$^{-/-}$ Sost$^{+/+}$ $n=8$, *Tfr2*$^{-/-}$ Sost$^{+/tg}$ $n=5$ and (**d**) bone formation rate/bone surface (BFR/BS) of 10-week-old female *Tfr2*$^{-/-}$ or WT mice containing one (*SOST*$^{+/tg}$) or no allele (*SOST*$^{+/+}$) of the *SOST* transgene (WT/Sost$^{+/+}$ $n=5$, WT/Sost$^{+/tg}$ $n=3$, *Tfr2*$^{-/-}$/Sost$^{+/+}$ $n=7$, *Tfr2*$^{-/-}$/Sost$^{+/tg}$ $n=6$). **b**–**d**, Two-way ANOVA with Bonferroni post hoc test was used for statistical analysis. **e**, *Sost* mRNA expression in ex vivo–differentiated osteoblasts from WT or *Tfr2*$^{-/-}$ mice after 24 h of anisomycin treatment (100 nM). ($n=3$ per group). One-way ANOVA with used for statistical analysis. **f**–**h**, 10-week-old male WT and *Tfr2*$^{-/-}$ mice were treated with 5 mg/kg anisomycin for 3 weeks. Shown are the (**f**) serum levels of sclerostin (WT/PBS $n=5$, WT/Aniso $n=4$, *Tfr2*$^{-/-}$/PBS $n=4$, *Tfr2*$^{-/-}$/Aniso $n=5$). **g**, Number of osteoblasts/bone perimeter (N.Ob/B.Pm) ($n=6$ per group) and (**h**) BV/TV of the fourth lumbar vertebrae ($n=5$ per group). **i**,**j**, Overexpression of ERK2 (pCMV6-Mapk1) and p38α (pCMV6-Mapk14) in day 7 WT and *Tfr2*$^{-/-}$ osteoblasts. *Sost* expression was analysed after 48 h and normalized to β-actin ($n=3$). **f**–**j**, Two-way ANOVA with Bonferroni post hoc test was used for statistical analysis. All data are presented as mean ± s.d. $^{*}P<0.05$, $^{**}P<0.01$, $^{***}P<0.001$. **k**, Scheme of Tfr2 actions in osteoblasts: Tfr2 binds BMPs and either directly activates BMP/MAPK signalling (1) or activates them via binding to BMPR (2) to induce the transcription of *Sost* and *Dkk1*. Secreted sclerostin acts as a Wnt antagonist and inhibits bone formation and decreases bone mass.

Tfr2 is a novel interaction partner of BMPs. Finally, we asked how Tfr2 can lead to impaired BMP-MAPK signal transduction in osteoblasts and thus explored whether Tfr2 can act as a BMP receptor. We generated a protein fragment containing the extracellular domain of Tfr2 (Tfr2-ECD), confirmed using SDS–polyacrylamide gel electrophoresis (SDS–PAGE) and western blot (Supplementary Fig. 8a), and performed surface plasmon resonance (SPR) analysis. Tfr2-ECD immobilized on sensor-chip-bound BMP-2, BMP-4, BMP-6, and BMP-7 more avidly than holo-Tf (Fig. 6a and Supplementary Fig. 8b), the only known Tfr2 ligand[10]. BMP-2, BMP-4, and BMP-6 also bound Tfr2-ECD at high salt concentrations, which were used to reduce nonspecific binding, although with a lower binding response (Supplementary Fig. 8c). Tfr2-BMP binding was further verified via an inverse approach using Tfr2-ECD as an analyte and BMP-2 or BMP-4 immobilized on the sensor chip (Supplementary Fig. 8d,e). Using this approach, we determined K_d values for Tfr2–BMP-2 (488.0 ± 37.0 nM) and Tfr2–BMP-4 (409.1 ± 39.0 nM) binding via steady-state analysis. Holo-Tf bound to Tfr2 at micromolar concentrations, suggesting a K_d value in the micromolar range (Supplementary Fig. 8f). Holo-Tf and BMP-2 did not compete for binding to Tfr2, as the sequential injection of either BMP-2 then holo-Tf or holo-Tf then BMP-2 did not change the initial binding response (Supplementary Fig. 8g,h). Interestingly, concomitant injection of BMP-2 and holo-Tf led to a much stronger binding response to Tfr2 than either analyte alone (Fig. 6b). As BMPs normally signal through a receptor complex consisting of the type I and type II BMP receptors, we tested whether BMP receptors (BMPRs) bind to Tfr2-ECD. Both BMPR-IA and BMPR-II had binding responses weaker than those of BMPs (Fig. 6a and Supplementary Fig. 8i). The physical interaction of Tfr2 and BMPR-IA was further

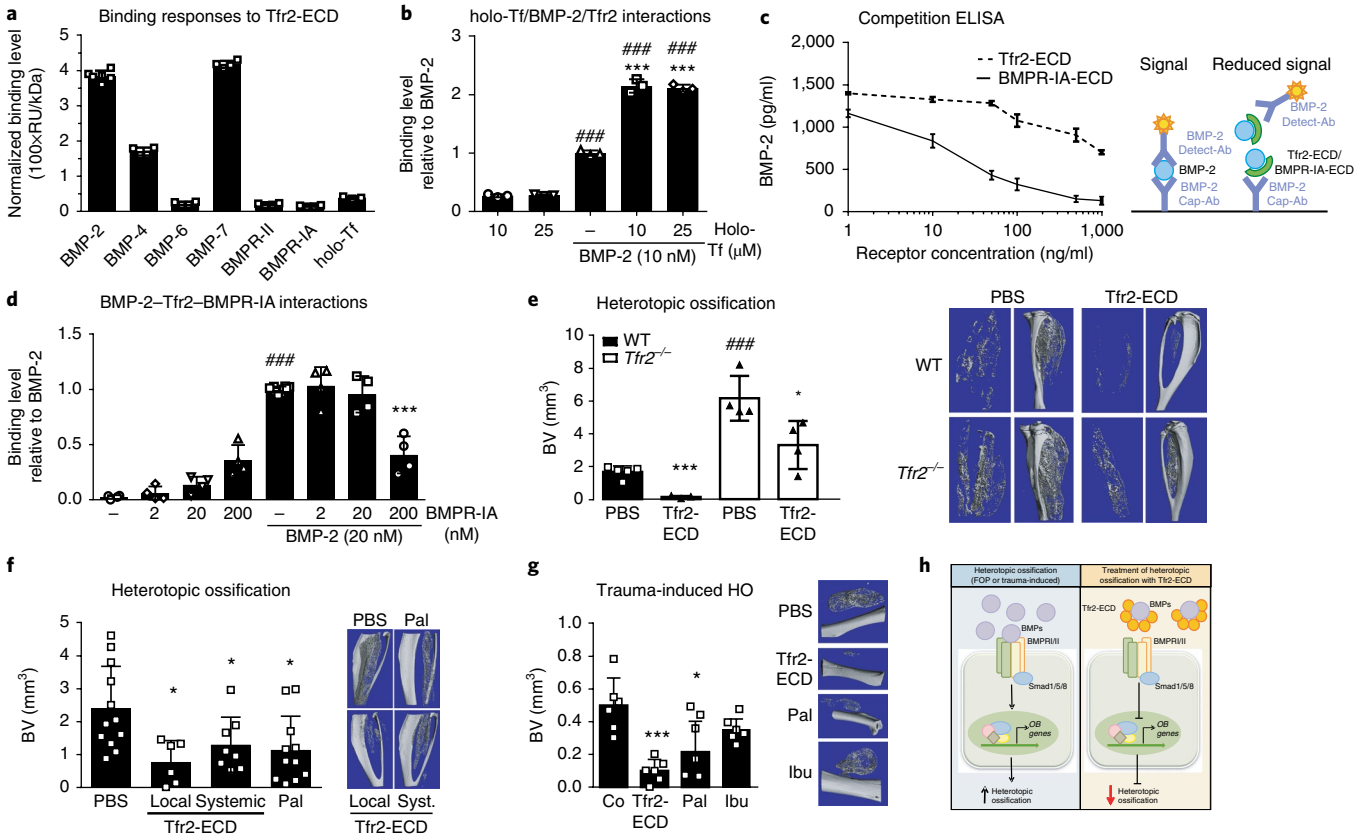

Fig. 6 | Tfr2 binds BMP ligands and blocks heterotopic ossification. a,**b**, Surface plasmon resonance (SPR) experiments using Tfr2-ECD immobilized on the sensor chip and 1 mg/ml holo-Tf, different BMP ligands (50 nM), or 200 nM BMP receptors as analytes. All experiments were performed three independent times. **a**, Quantification of the binding level normalized to the molecular weight (BMP-2 $n=6$, BMP-4, BMP-6, BMP-7, BMPR-II and BMPR-IA, $n=4$ per group; holo-Tf $n=3$). **b**, Binding response of different concentrations of holo-Tf and/or BMP-2 ($n=3$; $^{###}P<0.001$ vs. holo-Tf alone; $^{***}P<0.001$ vs. BMP-2 alone). **c**, Competitive BMP-2 sandwich ELISA was performed to test Tfr2-ECD (or BMPR-IA as a positive control) binding to BMP-2. A defined concentration of BMP-2 (1,500 pg/ml) was used with increasing concentrations of Tfr2-ECD and BMPR-IA. The principle of the assays is shown in the right schematic. $n=4$. **d**, SPR analyses. BMP-2 was injected either alone or with increasing concentrations of BMPR-IA. Binding response is relative to BMP-2 alone ($n=4$; $^{###}P<0.001$ vs. BMPR-IA alone; $^{***}P<0.001$ vs. BMP-2 alone). **b**,**d**, One-way ANOVA was used for statistical analysis. **e**, HO in 12-week-old female WT and *Tfr2*$^{-/-}$ mice after 3 weeks quantified by μCT (without the bone volume of the tibia). Representative images are shown on the right (WT PBS $n=5$, WT Tfr2-ECD $n=3$, *Tfr2*$^{-/-}$ PBS $n=4$, *Tfr2*$^{-/-}$ Tfr2-ECD $n=4$; $^{*}P<0.05$; $^{***}P<0.001$ to respective PBS control; $^{###}P<0.001$ vs. WT). Two-way ANOVA with Bonferroni post hoc test was used for statistical analysis. **f**, HO in 12-week-old female WT mice after 2 weeks quantified by μCT (without the bone volume of the tibia) (PBS $n=12$, local Tfr2-ECD $n=6$, systemic Tfr2-ECD $n=8$, Pal $n=11$; $^{*}P<0.05$ vs. PBS control). **g**, Trauma-induced heterotopic ossification (HO) model in 12-week-old female WT mice. HO after three weeks assessed using μCT. Pal, palovarotene; Ibu, ibuprofene. $n=6$ per group; $^{*}P<0.05$, $^{***}P<0.001$ vs. PBS control. **f**,**g**, One-way ANOVA was used for statistical analysis. All data are presented as mean ± s.d. **h**, Scheme of the mode of action of the Tfr2-ECD in the treatment of HO. Left, HO is induced by overactive BMP signalling, leading to the induction of osteoblastic genes and bone formation. Right, Tfr2-ECD neutralizes BMPs, preventing them from activating BMP signalling. Thus, osteoblastic bone formation is inhibited.

investigated using a cell system in which they were both overexpressed. Their interaction was confirmed by coimmunoprecipitation and was not affected by the presence of BMP-2 (Supplementary Fig. 8j). BMP-2 binding to the Tfr2-ECD was further verified using a competitive sandwich ELISA with BMPR-IA as a control (Fig. 6c). Additional SPR experiments revealed that BMPR-IA competes with Tfr2 for BMP-2 binding, as adding increasing concentrations of BMPR-IA reduced binding of BMP-2 to Tfr2-ECD (Fig. 6d). Of note, high nanomolar concentrations of BMPR-IA were required for competing with Tfr2–BMP-2.

We validated the BMP ligand binding property of Tfr2-ECD in vivo using a heterotopic ossification model. In this model, BMP-2 is injected into the anterior tibialis muscle of mice, which leads to muscular ossification[32]. Whereas injection of BMP-2 alone led to heterotopic ossification of the muscle in WT mice, the addition of Tfr2-ECD completely abrogated this effect (Fig. 6e and Supplementary Fig. 9a,b), suggesting that Tfr2 binds BMP-2 and prevents it from binding to its cognate BMPR. Similar experiments in *Tfr2*$^{-/-}$ mice demonstrated increased heterotopic ossification after BMP-2 injection compared with WT mice, which was significantly inhibited by co-application of Tfr2-ECD (Fig. 6e and Supplementary Fig. 9a,b). Thus, in addition to confirming functional BMP-binding activity of the Tfr2-ECD in vivo, these data emphasise the role of Tfr2 as a negative regulator of ossification in a BMP-dependent context.

Tfr2-ECD potently inhibits heterotopic ossification in two distinct preclinical models. Due to the robust effect of the Tfr2-ECD in diminishing BMP-2-induced heterotopic ossification, we compared Tfr2-ECD with palovarotene, a selective retinoic acid receptor-γ agonist that indirectly inhibits BMP signalling[33] and is currently under clinical investigation for the treatment of FOP. We

tested Tfr2-ECD as a single local treatment into the muscle and as a systemic treatment (intraperitoneal injections every other day). Both regimens reduced BMP-2-induced heterotopic ossification in WT mice after two weeks, with similar efficacy to that of daily palovarotene administration (Fig. 6f). Investigation of the chondrogenic phase of heterotopic ossification at day 8 in WT mice revealed that both systemic Tfr2-ECD and palovarotene treatment suppressed the number of chondrocytes and production of cartilage (Supplementary Fig. 9c,d). No adverse effects of systemic Tfr2-ECD treatment were observed on blood counts, iron parameters, bone homeostasis or the gross morphology of internal organs (Supplementary Table 3). Finally, we tested both compounds in a model of trauma-potentiated heterotopic ossification, a frequent complication after trauma, blast injuries, or hip replacement surgeries. A single dose of Tfr2-ECD inhibited new bone formation in the muscle, comparable to palovarotene (Fig. 6g). Daily treatment with ibuprofen, a frequent treatment of heterotopic ossification after hip surgeries[34], did not prevent trauma-induced heterotopic ossification (Fig. 6g). These data indicate that Tfr2-ECD is a potent inhibitor of heterotopic ossification and represents a potential new therapeutic strategy for treating disorders of excessive bone formation.

Discussion

Using a series of genetically modified mice and in vitro analyses, we identified a new role for Tfr2 as a modulator of BMP and Wnt signalling in osteoblasts. Tfr2 interacts with BMP ligands and receptors, activates p38MAPK signalling, and induces expression of the Wnt inhibitor *Sost*, blocking canonical Wnt signalling and thereby limiting bone formation and bone mass accrual (Fig. 5k). Furthermore, exploiting the BMP-binding property of the Tfr2-ECD in the form of a decoy receptor shows promise as a novel therapeutic strategy to prevent heterotopic ossification (Fig. 6h), which is of particular interest, as there are currently no specific treatments for congenital or trauma-induced heterotopic ossification.

Aside from its well-known function in the regulation of systemic iron levels[6–9], Tfr2 also ensures proper erythropoiesis[8,22,23]. Our study has now identified a novel extrahepatic role of Tfr2, control of bone mass via direct action in osteoblasts, though minor effects in myeloid cells, including early osteoclasts, cannot be excluded. This function appears to be a unique property of Tfr2 among the other iron-regulating proteins, as all other investigated mouse models of haemochromatosis display low bone mass. Accordingly, other studies have shown low bone mass in patients with *HFE*-dependent haemochromatosis[3] and in *Hfe*- and hepcidin-deficient mice[35,36]. In both cases, suppressed bone formation was proposed as the main underlying mechanism of low bone mass[35,37]. However, as both *Hfe*- and hepcidin-deficient mice are iron overloaded, it is unclear whether the low bone mass is an indirect result of the negative effects of iron overload or whether *Hfe* and hepcidin act directly in bone cells. Importantly, the high bone mass in *Tfr2*-deficient mice was independent of the iron status and the hepatic function of Tfr2, indicating Tfr2 has distinct roles in osteoblasts (control of matrix production) and hepatocytes (regulation of hepcidin expression and systemic iron homeostasis).

Even though Tfr2 has been known as a regulator of iron homeostasis for over 15 years, its mechanisms of action have remained elusive. Decreased levels of Smad1, Smad5, and Smad8 and MAPK/ERK signalling in *Tfr2*-deficient hepatocytes suggested that BMP signalling may be involved[11,13,38], but it remained unclear how Tfr2 activates BMP signalling. Previous studies in hepatocytes have suggested that Tfr2 forms a ternary complex with Hfe and hemojuvelin to activate hepcidin expression[12]. Our data, however, provide in vitro and in vivo evidence that demonstrates that Tfr2 can bind BMPs directly and activate downstream signalling. Binding of BMP-2 to Tfr2 was more than tenfold higher than that of holo-Tf, the only known ligand for Tfr2 (ref. [10]). Compared with BMP–BMPR interactions[39,40], BMP–Tfr2 binding affinity was markedly lower, suggesting that Tfr2 may act to fine-tune BMP signalling. As our studies also showed a direct interaction of Tfr2 with BMPRs, it remains to be investigated whether Tfr2 binds BMPs alone or within a multireceptor complex with BMPRs and/or other BMP co-receptors. Despite these first indications of Tfr2 being a BMP (co)-receptor, additional experiments will be required to define accurate binding affinities that account for stoichiometry, the possibility of receptor dimerization or oligomerization, and Tfr2-ECD purity. Interestingly, the combination of holo-Tf and BMP-2 bound much more avidly to Tfr2 than either holo-Tf or BMP-2 alone, suggesting that holo-Tf may exhibit considerable Tfr2 binding only in the presence of BMPs. This may be of particular importance, as hepatic endothelial cells have been identified as the main producers of BMP-2 and BMP-6 that act locally on hepatocytes to control hepcidin expression and iron homeostasis[41,42]. While hemojuvelin has been known to transmit the signal of BMP-6 to modulate hepcidin expression, BMP-6 can still induce hepcidin expression in hemojuvelin knock-out mice[43], suggesting that other receptors must be involved. Thus, the newly identified BMP-binding properties of Tfr2 may represent the missing link in the regulation of hepcidin via BMPs.

Our study further showed that BMP downstream signalling, in particular the BMP-p38MAPK pathway, is impaired in *Tfr2*$^{-/-}$ osteoblasts, resulting in reduced expression of the canonical Wnt inhibitors *Dkk1* and *Sost*, which are both potent negative regulators of bone formation[44–46]. Recent work has shown that BMP-2 stimulates expression of *Dkk1* and *Sost* by activating BMP-dependent Smad signalling and, in the case of *Dkk1*, through MAPK signalling via ERK and p38 (refs [30,47]). More-recent studies, including our own, show that *Sost* expression is also induced by p38MAPK signalling in osteoblasts[30,48]. Accordingly, anisomycin treatment, which activates all three MAPKs[49], rescued *Sost* expression and restored bone mass in *Tfr2*$^{-/-}$ mice. Similar to the phenotype of *Tfr2*$^{-/-}$ mice and counterintuitive to the supportive role of BMP signalling in osteoblastic bone formation, targeted disruption of *Bmpr1a* or *Acvr1* in osteoblasts impairs expression of *Sost* and results in high bone mass[47,50]. Additionally, treatment of *Bmpr1a*-deficient calvaria with recombinant sclerostin ex vivo restored normal bone morphology[47], similarly to overexpression of *SOST* in *Tfr2*$^{-/-}$ mice reducing bone volume to WT levels. However, *Tfr2*-deficient mice do not fully phenocopy the skeletal phenotype of *Bmpr1a*- or *Sost*-deficient mice. With osteoblast- and osteocyte-specific knock-out strains, deletion of *Tfr2*, *Sost*, and *Bmpr1a* leads to high bone mass. However, whereas *Bmpr1a*-conditional knock-out mice have low bone turnover[30,47,51], *Tfr2*-conditional knock-out mice have a high bone formation rate and normal osteoclast parameters, and *Sost*-conditional knock-out mice have a high bone formation rate[52]. Osteoclast parameters have not been reported in *Sost*-conditional knock-out mice, but are normal in *Sost*$^{-/-}$ mice[44]. Whereas an increase in bone formation appears to be the predominant mechanism of high bone mass in *Tfr2*- and *Sost*-conditional knock-out mice, the main driver of high bone mass in *Bmpr1a*-conditional knock-out mice appears to be reduced osteoclastogenesis due to a low RANKL-to-OPG ratio in osteoblasts[30,47]. This mechanism was reported to be independent of Wnt signalling, as overexpression of *Sost* did not rescue the osteoclast phenotype in *Bmpr1a*-conditional knock-out mice[47]. By contrast, *Tfr2*$^{-/-}$ mice have elevated osteoclast numbers and an increased RANKL-to-OPG ratio (WT, 0.225 ± 0.046; *Tfr2*$^{-/-}$, 0.696 ± 0.120; $n = 4$, $P = 0.0003$), but, similar to *Bmpr1a*-conditional knock-out mice, this phenotype was not rescued by *Sost* overexpression. Interestingly, deficiency of *Bmpr2* in osteoblasts results in high bone mass accompanied by a high bone formation rate and normal bone resorption[53], suggesting that Tfr2 shares more similarities with Bmpr2 than Bmpr1a. Finally, *Bmpr1a*-conditional knock-out mice have disorganised bone matrix, leading to reduced bone

strength[54,55]. This finding is in contrast with *Tfr2*$^{-/-}$ and *Sost*$^{-/-}$ mice, which both have normal bone matrix organization and increased bone strength[44]. Despite similarities that propose Tfr2 acts in a similar way or even in conjunction with BMPRs, additional pathways appear to mediate its effects on bone, independent of BMP signalling. Thus, Tfr2 is clearly a critical regulator of *Sost* expression in osteoblasts and provides another link between BMP and Wnt signalling.

Finally, we show that the ability of the Tfr2-ECD to bind BMPs and act as a decoy receptor reduces heterotopic ossification in two distinct preclinical models. Heterotopic ossification is a serious and common medical complication after blast injuries, such as those found in soldiers and civilians, burn victims, and recipients of total hip endoprostheses. Up to 30% of patients undergoing hip replacement surgery and 50% of severely wounded soldiers develop heterotopic ossification[56,57]. Extensive heterotopic ossification is also a hallmark of FOP, a rare human disease caused by an activating mutation in the gene encoding a BMP type I receptor, *ACVR1* (ref. [21]). Since the identification of this mutation, BMP signalling has been implicated in the pathogenesis of heterotopic ossification. To date, therapeutic options for FOP and trauma-induced heterotopic ossification are limited. Radiation and nonsteroidal antirheumatic drugs are frequently used to inhibit surgery-induced heterotopic ossification, with varying success[34]. In our study, ibuprofen did not significantly reduce heterotopic ossification. In FOP, glucocorticoids are used to reduce inflammation during flare-ups. However, they do not block progressive ossification. Rapamycin, anti-activin antibodies, and palovarotene have recently been shown to reduce heterotopic ossification in preclinical models of FOP via different mechanisms[33,58–60]. Palovarotene indirectly interferes with the BMP pathway and is currently the only drug under clinical investigation. Both local and systemic treatment with Tfr2-ECD inhibited heterotopic ossification to a similar extent as palovarotene. Systemic treatment with Tfr2-ECD did not show adverse effects on iron or bone metabolism within the 2-week treatment period, which is of relevance, as mice lacking *Tfr2β*, which has a similar structure to that of Tfr2-ECD, have increased iron levels in the spleen[8]; therefore, differences in iron metabolism may have been anticipated. In the future, longer and more extensive pharmacological studies are required to conclusively address the safety profile of Tfr2-ECD.

Taken together, our findings uncovered Tfr2 as a novel regulator of bone mass via modulation of the BMP-p38MAPK-Wnt signalling axis and identified Tfr2-ECD as a promising therapeutic option to treat heterotopic ossification and disorders of excessive bone formation.

Methods

Mice. Generation of *Tfr2*$^{-/-}$ mice and *Tfr2* knock-in (*Tfr2*-KI) mice, which lack only the *Tfr2β* isoform, were described previously[8]. Conditional *Tfr2* knock-out mice were generated on the background of the *Tfr2*-KI mouse (129×1/svJ), thereby generating cell-type-specific *Tfr2α* knock-out mice that also lack *Tfr2β* globally. Liver-specific *Tfr2*-knock-out (LCKO) mice were generated using albumin-Cre (sv129 background). To delete *Tfr2α* in osteoblast precursors, the doxycycline-repressible osterix-Cre (*Osx-cre*) was used[61]. Breeding pairs and mice up to the age of 5 weeks were kept on doxycycline (0.5 g/l). For the deletion of *Tfr2α* in mature osteoclasts, the cathepsin K Cre (*Ctsk-cre*) was used[62]. Lysozyme M Cre (*Lysm-cre*) was used for deletion of *Tfr2* in early osteoclasts[63]. *Tfr2*$^{f/f}$;*Osx-cre, Tfr2*$^{f/f}$;*Lysm-cre*, and *Tfr2*$^{f/f}$;*Ctsk-cre* mice were generated on a mixed sv129/C57BL/6 background. Littermates were used as controls.

To obtain *Tfr2*-deficient mice with an overproduction of human sclerostin, *Tfr2*$^{-/-}$ mice were crossed with *Dmp1-SOST* transgenic mice to obtain *Tfr2*$^{-/-}$;*Dmp1-SOST*$^{+/tg}$ mice[64]. The production of ferroportin knock-in mice with a point mutation (C326S) and *Hfe* knock-out mice were described previously[26,27]. All mice were routinely genotyped using standard PCR protocols.

In vivo experiments. All animal procedures were approved by the institutional animal care committee TU Dresden and the Landesdirektion Sachsen. All mice were fed a standard diet with water *ad libitum* and were kept in groups of five animals per cage. Mice were exposed to a 12 h light/dark cycle and an air-conditioned room at 23 °C (not specific-pathogen free). Enrichment was provided in the form of cardboard houses and bedding material. Mice were randomly assigned to treatment groups, and the subsequent analyses were performed in a blinded fashion.

Bone phenotyping. Male and female *Tfr2*$^{-/-}$ and wild-type mice at 10–12 weeks of age were used. For the characterization of *Tfr2*$^{-/-}$ mice, older mice (6 and 12 months) were also used. Male *Tfr2*$^{f/f}$;*Osx-cre* and *Tfr2*$^{f/f}$;*Ctsk-cre* and the corresponding cre-negative littermate controls were killed at 10–12 weeks of age for bone phenotype analysis.

Ovariectomy. Female 11- to 14-week-old WT or *Tfr2*$^{-/-}$ mice were bilaterally ovariectomized or sham operated. After 4 weeks, mice were killed for further analyses. Each group consisted of 5–10 mice.

Iron-rich diet. WT animals received a 2%-iron-enriched standard diet from weaning (14 days old) until euthanisation (8 weeks of treatment). There were four or five mice per group.

Iron-free diet. Male *Tfr2*$^{-/-}$ and WT mice received an iron-free diet (Envigo, Italy) from weaning until 10 weeks of age. Control mice received a standard diet containing 0.2 g iron/kg (GLOBAL DIET 2018, Envigo, Italy). There were nine mice per group.

Iron chelation. Ten-week-old male *Tfr2*$^{-/-}$ and WT mice received daily intraperitoneal injections of 250 mg/kg deferoxamine (Sigma, Germany, dissolved in PBS) or PBS for three weeks. This experiment was performed two independent times with 3–5 mice.

Full bone marrow transplantation. Bone marrow cells were isolated from 12-week-old male *Tfr2*$^{-/-}$ mice or WT controls. Two million cells were transplanted into lethally irradiated (8 Gy) male WT or *Tfr2*$^{-/-}$ mice via retro-orbital venous plexus injection. Engraftment efficiency was monitored every four weeks using flow cytometry. After 16 weeks, mice were sacrificed for bone analyses. This experiment was performed twice with 7–12 mice per group.

Anisomycin treatment. Female 11-week-old WT and *Tfr2*$^{-/-}$ mice were treated with 5 mg/kg anisomycin (intraperitoneally) 3×/week for three weeks. This experiment was performed twice with five mice per group.

Heterotopic ossification (HO). The HO model was performed according to Wosczyna et al.[32]. Briefly, 2.5 µl of 1 mg/ml recombinant BMP-2 (ThermoFisher) or 2.5 µl of 1 mg/ml Tfr2-ECD was mixed with 47.5 µl Matrigel (BD Bioscience) on ice. For the local combination treatment, 2.5 µl BMP-2 was mixed with 2.5 µl Tfr2-ECD and 45 µl Matrigel. The Matrigel mixtures were injected into the midbelly of the tibialis anterior muscle of 10-week-old female WT and *Tfr2*-deficient mice. Some mice were treated daily with palovarotene through oral gavage using a previously published protocol[58]. Palovarotene (Hycultec) was dissolved in DMSO and diluted 1:4 with corn oil. Mice received palovarotene at a dose of 100 µg/mouse for the first 5 d and 50 µg/mouse for the remainder of the experiment (days 6–14). Two weeks after BMP-2 injection, the legs were harvested for analysis. This experiment was performed three times with 3–11 mice per group.

To analyse the chondrogenic phase of HO, we performed the experiment as described above, but terminating on day 8. This experiment was performed once with four to six mice per group.

For systemic Tfr2-ECD treatment, WT mice were treated every other day with Tfr2-ECD intraperitoneally for two weeks. Mice received 250 µg Tfr2-ECD (10 mg/kg body weight) per injection for the first 10 d after BMP-2/Matrigel injection into the muscle and 125 µg per injection (5 mg/kg body weight) for the remaining time. This experiment was performed once with eight to ten mice per group.

Drop-weight HO. This experiment was performed according to Liu et al.[65] with minor modifications. Female 10- to 12-week-old WT mice were anaesthetized and placed on a ridge of a plastic container over which the right leg was bent so the femur was lying horizontally. Mice received an injection of 1 µg BMP-2 mixed in 50 µl Matrigel. Afterwards, a stainless-steel ball of 16 g (16 mm diameter) was dropped from a distance of 80 cm height onto the quadriceps muscle. Mice either received a single dose of 1 µg Tfr2-ECD, which was co-injected with the BMP-2/Matrigel mixture, or palovarotene (Hycultec), which was administered daily by oral gavage. Palovarotene was dissolved in DMSO and diluted 1:4 with corn oil. Mice received palovarotene at a dose of 100 µg/mouse for the first 5 d and 50 µg/mouse for the remainder of the experiment (days 6–21). One group of mice received ibuprofen via their drinking water at a dose of 100 mg/ml, which was changed every other day[66]. Mice received methimazole (200 mg/kg) to reduce pain for the entire duration of the experiment. This experiment was performed twice with six mice per group.

Micro-CT, bone micromineralization density, and biomechanical testing. Bone microarchitecture was analysed using the vivaCT40 (Scanco Medical, Switzerland).

The femur and the fourth lumbar vertebra were imaged at a resolution of 10.5 µm with X-ray energy of 70 kVp, 114 mA, and an integration time of 200 ms. The trabecular bone in the femur was assessed in the metaphysis 20 slices below the growth plate using 150 slices. In the vertebral bone, 150 slices were measured between both growth plates. The cortical bone was determined in the femoral midshaft (150 slices). Predefined scripts from Scanco were used for the evaluation.

Bone micromineralization densities were determined using quantitative backscattered electron-scanning electron microscopy (qBSE-SEM). Fourth lumbar vertebrae (L4) fixed in neutral buffered formalin from 12-week-old male mice were embedded in methacrylate. Longitudinal block faces were cut through specimens, which were then polished and coated with 25 nm of carbon using a high-resolution sputter coater (Agar Scientific Stanstead UK). Samples were imaged using backscattered electrons at 20 kV, 0.4 nA, and a working distance of 17 mm with a Tescan VEGA3 XMU (Tescan, Brno, Czech Republic) equipped with a Deben 24 mm four-quadrant backscatter detector (Deben, Bury St. Edmunds, UK). Bone mineralization densities were determined by comparison to halogenated dimethacrylate standards, and an eight-interval pseudocolor scheme was used to represent the graduations of micromineralization, as described previously[67].

Three-point bending of the femur was conducted to assess bone strength. The femurs were stored in 70% ethanol and rehydrated in PBS prior to testing. Mechanical testing was performed using the zwickiLine (Zwick, Germany). Load was applied to the anterior side of the femoral shaft to measure the maximum load at failure (F_{max}, N).

Bone histomorphometry. Mice were injected with 20 mg/kg calcein (Sigma) 5 d and 2 d before euthanisation. Dynamic bone histomorphometry was performed as described previously[68]. Briefly, the third lumbar vertebra and tibia were fixed in 4% PBS-buffered paraformaldehyde and dehydrated in an ascending ethanol series. Subsequently, bones were embedded in methacrylate and cut into 7-µm sections to assess the fluorescent calcein labels. Unstained sections were analysed using fluorescence microscopy to determine the mineralized surface/bone surface (MS/BS), the mineral apposition rate (MAR), and the bone formation rate/bone surface (BFR/BS), as well as the bone volume/total volume (BV/TV), trabecular number (Tb.N), trabecular separation (Tb.Sp), and trabecular thickness (Tb.Th).

To determine numbers of osteoclasts, the femur and fourth lumbar vertebra were decalcified for 1 week using Osteosoft (Merck), dehydrated, and embedded into paraffin. Tartrate-resistant acid phosphatase (TRAP) staining was used to assess the osteoclast surface per bone surface (Oc.S/BS). Bone sections were analysed using the Osteomeasure software (Osteometrics, USA) following international standards.

To assess HO using the haematoxylin and eosin staining, the calves (HO) and thighs (drop-weight) were decalcified, dehydrated, and embedded into paraffin. Limbs were cut into 2-µm sections and stained with haematoxylin and eosin. For von Kossa/van Gieson and Safranin O staining, legs were not decalcified; they were embedded into methacrylate and cut into 4-µm-thick sections.

Immunohistochemistry. For immunohistochemical analysis, paraffin sections from WT and *Tfr2*$^{-/-}$ bones were dewaxed, rehydrated, and heat retrieved of antigens. Endogenous peroxidase activity was blocked using 0.3% H_2O_2 in PBS for 10 min at room temperature, and nonspecific binding sites were blocked using the blocking buffer of the VECTASTAIN Elite ABC Kit (VECTOR Laboratories) for 45 min at room temperature. Afterwards, sections were incubated with an anti-Tfr2 antibody (H-140, Santa Cruz), a β-catenin antibody (Sigma-Adrich, cat. no. C2206) or an axin-2 antibody (#ab107613, Abcam) overnight at 4 °C. Subsequently, slides were treated with an anti-mouse secondary antibody conjugated to biotin and then developed using avidin-conjugated HRP with diaminobenzidine as substrate (Dako). Slides were examined using a Zeiss Axio Imager M.1 microscope. 200 cells were counted per slide and graded according to no staining (0), weak staining (1), and strong staining (2).

Measurement of iron content in liver and bone. The iron concentration in the liver was determined using 20 mg of dried liver tissue, as previously published[8]. The iron concentration in the bone was determined using atomic absorption spectroscopy (PerkinElmer Analyst 800) of dried bone tissue (bone-marrow-flushed femur and tibia), as previously published[69].

Serum analysis. The bone turnover markers C-terminal telopeptide (CTX) and pro-collagen type I N-terminal peptide (P1NP) were measured in the serum using ELISAs (IDS, Germany). Serum dickkopf-1 and BMP-2 were measured using ELISAs from R&D Systems (Germany). Mouse sclerostin was measured with an ELISA from Alpco (USA). Serum ferritin and iron were measured using routine methods for clinical analyses on a Roche Modular PPE analyser. The transferrin saturation was determined using a total iron binding capacity kit from Randox.

Primary osteoclast culture. Osteoclasts were generated from the bone marrow of WT mice and seeded at a density of 1×10^6 cells/cm^2. Alpha-MEM (Biochrom, Germany) with 10% FCS, 1% penicillin/streptomycin, and 25 ng/ml M-CSF (all from Life Technologies) was used for the first 2 d of differentiation. Afterwards, medium was supplemented with 30 ng/ml RANKL (Life Technologies) for the remainder of the culture (5–7 d). RNA was isolated at various time points, and mature osteoclasts were used for immunofluorescence analysis.

Primary osteoblast culture. Primary murine osteoblasts were differentiated from the bone marrow using standard osteogenic medium in DMEM with 10% FCS, 1% penicillin/streptomycin (Life Technologies, Germany). RNA was isolated at various time points, and day 7 osteoblasts were used for immunofluorescence analysis of Tfr2 and the deep-sequencing analysis.

Signalling studies. Day 7–differentiated cells were treated with 50 ng/ml BMP-2, BMP-4 or BMP-6 for 0, 20, and 40 min and lysed in protein lysis buffer (at least two independent experiments with $n = 3$ each for each group). Anisomycin was used to activate MAPK signalling on day 7–differentiated osteoblasts. Cells were treated with 100 nM anisomycin for 20 min for subsequent protein analysis. For RNA isolation and detection of gene expression, cells were treated with different doses (10 and 100 nM) of anisomycin for 24 h (two independent experiments with $n = 3$ for each group).

Overexpression. 1 µg of the pcDNA3.1 vector containing the murine *Tfr2* gene was transfected into 70–80% confluent cells using Fugene HD (Roche)[8]. An empty pcDNA3.1 vector was used as a control. Additionally, the overexpression vectors pCMV6-MAPK1 (ERK2), pCMV6-MAPK14 (p38), pCMV6-Smad1, and pCMV6-Smad4 were purchased from Origene to overexpress the respective signalling proteins. The pCMV6-Entry vector was used as control. Each experiment was performed once with cells from four different mice.

RNA isolation, reverse transcription, and real-time PCR. RNA from cell cultures was isolated with the High Pure RNA Isolation Kit (Roche), and RNA from the bones of mice was isolated by crushing flushed bones (femur and tibia) in liquid nitrogen and collecting the bone powder in Trifast (Peqlab, Germany). Other organs were homogenized directly in Trifast using an ULTRA-TURRAX (IKA, Germany). 500 ng RNA was reverse transcribed using Superscript II (Invitrogen, Germany) and subsequently used for SYBR green–based real-time PCR using a standard protocol (Life Technologies). The results were calculated using the ΔΔCT method and are presented in *x*-fold increase relative to *β-actin* (or *GAPDH* where indicated) mRNA levels.

Protein isolation and western blot. Cells were lysed in a buffer containing 20 mM Tris/HCl, pH 7.4, 1% SDS, and a protease inhibitor (complete mini, Roche, Germany). To isolate protein from tissues, the protein fraction of the Trifast procedure was used and further processed according to the manufacturer's protocol. The protein concentration was determined using the BCA method (Pierce, Germany). 20 µg of heat-denatured protein was loaded onto a 10% gel, separated, and transferred onto a 0.2-µm nitrocellulose membrane (Whatman, Germany). After blocking for 1 h with 5% non-fat dry milk or 2% BSA in Tris-buffered saline with 1% Tween-20 (TBS-T), membranes were incubated with primary antibodies to signalling proteins (Cell Signaling) overnight and washed three times with TBS-T. For the detection of Tfr2, the H-140 antibody from Santa Cruz (Germany) was used, which detects an epitope corresponding to amino acids 531–670. Other antibodies used were: lamin A/C (#sc-20681, Santa Cruz), connexin-43 (#3512, Cell Signaling), tubulin (#2146, Cell Signaling), and GAPDH (#5G4, HytestH). Thereafter, membranes were incubated with the appropriate HRP-conjugated secondary antibodies for 1 h at room temperature. Finally, membranes were washed with TBS-T and incubated with an ECL substrate (ThermoFisher Scientific). The proteins were visualized using the MF-ChemiBIS 3.2 bioimaging system (Biostep, Germany). All unprocessed western blot images are shown in Supplementary Figs. 10 and 11.

Subcellular protein fractionation. For separation of cytoplasmic, membrane, and nuclear protein extracts of osteoblasts, primary murine osteoblasts were differentiated from the bone marrow of three WT mice. At day 7, cells were harvested, and the subcellular protein fractions were isolated using the subcellular protein fractionation kit (ThermoFisher Scientific) according to manufacturer's recommendation.

Immunofluorescence staining. For immunofluorescence staining, cells were grown on glass slides. At the desired time point, cells were fixed with 100% methanol for 15 min, permeabilised with 0.5% Triton X-100 for 10 min and, after three washes, blocked with 1% BSA in PBS for 30 min. Afterwards, cells were incubated with an anti-mouse Tfr2 antibody (H-140, Santa Cruz) overnight at 4 °C. After being washed, cells were stained with an anti-mouse osterix antibody (sc-393325, Santa Cruz) or phalloidin at room temperature for 1 h. Subsequently, cells were washed and incubated for 1 h with an Alexa Fluor 488– or Alexa Fluor 594–labelled secondary antibody (Life Technologies), washed, and stained with DAPI for 5 min. After being washed again, glass slides were embedded in a small droplet of mounting medium (Dako). Slides were examined using a Zeiss LSM 510 confocal microscope (Zeiss EC Plan-Neofluar 40×/1.3 oil), and photographs were taken and processed with the Zen 2009 software.

Coimmunoprecipitation. Human hepatoma cells (HuH7) were transfected with 7.5 µg of pCMV-3XFLAG-BMPR-IA and 7.5 µg pcDNA3-TFR2-HA or pcDNA3-LDLR-HA using TransIT-LT1 Transfection Reagent (Mirus Bio LLC) following the manufacturer's protocol. 48 h after transfection, cells were treated with 50 ng/ml of BMP-2 (Peprotech) for 1.5 h, where indicated. Cell lysates were incubated with pre-equilibrated anti-FLAG M2 affinity gel (Sigma Aldrich) at 4 °C for 2 h. Samples were then eluted with 50 µl of lysis buffer containing 300 µg/ml 3× FLAG Peptide (Sigma Aldrich). 10% of the total lysate was used as input (In). Immunorecognition was visualized using αFLAG and αHA antibodies (1:1,000, Sigma Aldrich; cat. nos. H9758, F7425).

Next-generation sequencing and data analysis. Total RNA was isolated from day 7–differentiated cells of *Tfr2*$^{-/-}$ and WT mice using Trifast. RNA quality was assessed using the Agilent Bioanalyzer, and total RNA with an integrity number ≥9 was used. mRNA was isolated from 1 µg total RNA using the NEBNext Poly(A) mRNA Magnetic Isolation Module according to the manufacturer's instructions. After chemical fragmentation, samples were subjected to strand-specific RNA-sequencing library preparation (Ultra Directional RNA Library Prep, NEB). After ligation of adaptors (Oligo1, 5′-ACA CTC TTT CCC TAC ACG ACG CTC TTC CGA TCT-3′; Oligo 2, 5′-P-GAT CGG AAG AGC ACA CGT CTG AAC TCC AGT CAC-3′), residual oligos were depleted using bead purification (XP, Beckman Coulter). During subsequent PCR enrichment (15 cycles) libraries were indexed (Primer 1: Oligo_Seq AAT GAT ACG GCG ACC ACC GAG ATC TAC ACT CTT TCC CTA CAC GAC GCT CTT CCG ATC T; primer 2: GTG ACT GGA GTT CAG ACG TGT GCT CTT CCG ATC T; primer 3: CAA GCA GAA GAC GGC ATA CGA GAT NNNNNN GTG ACT GGA GTT). After final purification (XP beads), libraries were quantified (Qubit dsDNA HS Assay Kit, Invitrogen), equimolarly pooled, and distributed on multiple lanes for 75-bp single-read sequencing on an Illumina HiSeq 2500 and an Illumina NextSeq 500.

After sequencing, FastQC (http://www.bioinformatics.babraham.ac.uk/) was used for basic quality control. Reads were then mapped onto the mouse genome (mm10) using GSNAP (version 2014-12-17) together with known splice sites (Ensembl v75) as support. Library diversity was assessed by investigating the redundancy in the mapped reads. A table with counts per gene was obtained by running featureCounts (v1.4.6) on the uniquely mapped reads using Ensembl v75 gene annotations. Normalisation of the raw read counts based on the library size and testing for differential expression between KO and WT was performed with the R package DESeq2 (v1.6.3). Genes with an adjusted (Benjamini–Hochberg) *P* value <0.05 were considered as differentially expressed.

Gene ontology analyses were performed with Cytoscape 3.2.1 and the ClueGO plugin. Only significantly ($P<0.05$) up- or downregulated genes were fed into the analyses. Gene Set Enrichment Analysis (GSEA) was carried out using the Broad Institute GSEA software "GseaPreRanked" tool (nperm = 1,000, set_min = 5, set_max = 500, scoring_scheme = weighted) to analyse a list of 18,106 nonredundant gene symbols ranked by their $\log_2$ fold-change of expression between *Tfr2*$^{-/-}$ and WT conditions. In total, 58 gene sets were used for the analysis, including 50 Hallmark gene sets[70], three osteoblast-specific gene sets from Park et al.[71] and five other gene sets from Sanjuan-Pla et al.[72].

Expression of the Tfr2 extracellular domain. The coding sequence of the full-length extracellular domain (ECD, amino acids 103–798) of murine Tfr2 was synthesised by Genscript (Germany). Recombinant His-MBP-c3-Tfr2-ECD was expressed in *Sf9* insect cells using the baculovirus expression system (pOCC211-Tfr2-ECD). Culture supernatant (5 litres) was harvested, filtered, and loaded on a HisTrap column, and after extensive wash with PBS, the Tfr2-ECD protein was eluted using PBS with 250 mM imidazole. The yield in the first protein production was 40 mg Tfr2-ECD, and the yield in the second protein production was 46 mg Tfr2-ECD. Presence of Tfr2 was analysed using Coomassie staining of SDS–PAGE with reducing conditions and western blot.

Experiments were repeated with a commercially produced Tfr2-ECD from Cusabio. This commercial fragment also contained the entire ECD (amino acids 103–798), and was dissolved in PBS only.

Surface plasmon resonance binding and kinetic analysis. Interactions of the Tfr2-ECD and holo-Tf, BMP ligands (BMP-2, BMP-4, BMP-6, and BMP-7, R&D Systems) and BMP receptors (BMPR-IA, BMPR-II, R&D Systems) were analysed using a Biacore T100 instrument (GE Healthcare). Tfr2-ECD, BMP-2, and BMP-4 were immobilised onto Series S Sensor Chips C1 (GE Healthcare) via its amine groups at 25 °C. The carboxyl groups on the chip surface were activated for 7 min with a mixture containing 196 mM 1-ethyl-3-(3-dimethylaminopropyl) carbodiimide hydrochloride and 50 mM *N*-hydroxysuccinimide at a flow rate of 10 µl/min. Next, 5 µg/ml of Tfr2-ECD diluted in sodium acetate buffer (pH 4.5) or 2 µg/ml BMP-2 or BMP-4 was injected at a flow rate of 5 µl/min until immobilization levels of approximately 200 RU (Tfr2-ECD) or 100 RU (BMP-2 and BMP-4) were achieved. Unreacted groups were deactivated via injection of 1 M ethanolamine-HCl, pH 8.5 (7 min, 10 µl/min). A reference surface was created according to the same protocol but omitting the Tfr2 injection.

The binding analysis was performed at 37 °C at a flow rate of 30 µl/min. Each analyte was diluted in running buffer (HBS-P (pH 7.4), 150 mM NaCl, supplemented with 50 nM $FeCl_3$). In some experiments, 500 mM NaCl was used to reduce potential nonspecific binding. BMP ligands were used at the indicated concentrations (0–50 nM). BMP receptors were used at a concentration of 2–200 nM, holo-Tf at 2.5–100 µM, and Tfr2-ECD at 10–5,000 nM. In some experiments, BMP-2–BMPR-IA and BMP-2–holo-Tf were injected at the same time. Concentration-dependent binding of holo-Tf was performed without intermediate regeneration.

For binding analysis, an injection of analyte for 240 s or 300 s over a Tfr2-ECD surface was followed by a 1,000-s dissociation. The values of the binding levels were recorded from referenced signals 10 s before the end of the injection relative to baseline response, then emended for the respective molecular weight. After dissociation for 1,000 s, the chip surface was regenerated for 60 s with 5 M NaCl, 50 mM NaOH in HBS-P, followed by a 1,000-s stabilization.

Single-cycle kinetics with five sequential analyte injections was carried out with a sensitivity-enhanced Biacore T200 (GE Healthcare) to determine the K_d range of Holo-Tf/Tfr2 and the dissociation rates, k_{off} (complex stabilities), for Tfr2 binding to BMP-2 and BMP-4 surfaces. The kinetic fitting was performed by global fitting using the 1:1 Langmuir binding model (A + B = AB). Steady-state analyses were conducted to determine the affinities (K_d). Therefore, a 1:1 interaction of Tfr2 with BMP-2 or BMP-4 was assumed by fitting the measured binding responses at equilibrium against the concentration. To achieve a robust fit and the typical curvature of the plot, a wide range of Tfr2 concentrations was analysed (10–5,000 nM). Binding and kinetic parameters were evaluated with Biacore T200 evaluation software 3.1.

BMP-2 competitive ELISA. We used the Duo Set BMP-2 ELISA kit from R&D Systems for BMP-2 competitive ELISA assays. After coating the plate with the BMP-2 capture antibody overnight, 1.5 ng/ml BMP-2 was added with increasing concentrations of the Tfr2-ECD or the BMPR-IA (positive control, R&D Systems). After 1 h of incubation at room temperature RT and extensive washing, the detection antibody was added according to the manufacturer's protocol, and the amount of BMP-2 was quantified. This experiment was performed at least three independent times.

Statistical analysis. Data are presented as mean ± standard deviation (SD). Graphs and statistics were prepared using GraphPad Prism 6.0 software. Normality of data was determined using the Kolmogorov–Smirnov test. In cases where data were normally distributed, statistical evaluations of two group comparisons were performed using a two-sided Student's *t* test. One-way analysis of variance (ANOVA) was used for experiments with more than two groups. Two-way ANOVA with Bonferroni post hoc tests were used for analysing genotype and treatment effects. If data were not normally distributed, the Mann–Whitney test and the Wilcoxon signed rank test were used for data analysis. Frequency distributions of micromineralization densities from qBSE-SEM grey-scale images were compared using the Kolmogorov–Smirnov test[67].

Reporting Summary. Further information on research design is available in the Nature Research Reporting Summary linked to this article.

Data availability

All data sets generated during the current study are available from the corresponding author upon reasonable request.

Received: 20 July 2018; Accepted: 19 October 2018;
Published online: 7 January 2019

References

1. Muckenthaler, M. U., Rivella, S., Hentze, M. W. & Galy, B. A red carpet for iron metabolism. *Cell* **168**, 344–361 (2017).
2. Imel, E. A. et al. Serum fibroblast growth factor 23, serum iron and bone mineral density in premenopausal women. *Bone* **86**, 98–105 (2016).
3. Guggenbuhl, P. et al. Bone mineral density in men with genetic hemochromatosis and HFE gene mutation. *Osteoporos. Int.* **16**, 1809–1814 (2005).
4. Nemeth, E. et al. Hepcidin regulates cellular iron efflux by binding to ferroportin and inducing its internalization. *Science* **306**, 2090–2093 (2004).
5. Powell, L. W., Seckington, R. C. & Deugnier, Y. Haemochromatosis. *Lancet* **388**, 706–716 (2016).
6. Camaschella, C. et al. The gene TFR2 is mutated in a new type of haemochromatosis mapping to 7q22. *Nat. Genet.* **25**, 14–15 (2000).
7. Fleming, R. E. et al. Targeted mutagenesis of the murine transferrin receptor-2 gene produces hemochromatosis. *Proc. Natl. Acad. Sci. USA* **99**, 10653–10658 (2002).
8. Forejtnikova, H. et al. Transferrin receptor 2 is a component of the erythropoietin receptor complex and is required for efficient erythropoiesis. *Blood* **116**, 5357–5367 (2010).
9. Wallace, D. F., Summerville, L., Lusby, P. E. & Subramaniam, V. N. First phenotypic description of transferrin receptor 2 knockout mouse, and the role of hepcidin. *Gut* **54**, 980–986 (2005).

10. Johnson, M. B. & Enns, C. A. Diferric transferrin regulates transferrin receptor 2 protein stability. *Blood* **104**, 4287–4293 (2004).
11. Poli, M. et al. Transferrin receptor 2 and HFE regulate furin expression via mitogen-activated protein kinase/extracellular signal-regulated kinase (MAPK/Erk) signaling. Implications for transferrin-dependent hepcidin regulation. *Haematologica* **95**, 1832–1840 (2010).
12. D'Alessio, F., Hentze, M. W. & Muckenthaler, M. U. The hemochromatosis proteins HFE, TfR2, and HJV form a membrane-associated protein complex for hepcidin regulation. *J. Hepatol.* **57**, 1052–1060 (2012).
13. Wallace, D. F. et al. Combined deletion of Hfe and transferrin receptor 2 in mice leads to marked dysregulation of hepcidin and iron overload. *Hepatology* **50**, 1992–2000 (2009).
14. Hogan, B. L. Bone morphogenetic proteins: multifunctional regulators of vertebrate development. *Genes Dev.* **10**, 1580–1594 (1996).
15. Andriopoulos, B. et al. BMP6 is a key endogenous regulator of hepcidin expression and iron metabolism. *Nat. Genet.* **41**, 482–487 (2009).
16. Babitt, J. L. et al. Bone morphogenetic protein signaling by hemojuvelin regulates hepcidin expression. *Nat. Genet.* **38**, 531–539 (2006).
17. Mayeur, C., Leyton, P. A., Kolodziej, S. A., Yu, B. & Bloch, K. D. BMP type II receptors have redundant roles in the regulation of hepatic hepcidin gene expression and iron metabolism. *Blood* **124**, 2116–2123 (2014).
18. Steinbicker, A. U. et al. Perturbation of hepcidin expression by BMP type I receptor deletion induces iron overload in mice. *Blood* **118**, 4224–4230 (2011).
19. Wang, R. H. et al. A role of SMAD4 in iron metabolism through the positive regulation of hepcidin expression. *Cell. Metab.* **2**, 399–409 (2005).
20. Yu, P. B. et al. Dorsomorphin inhibits BMP signals required for embryogenesis and iron metabolism. *Nat. Chem. Biol.* **4**, 33–41 (2008).
21. Shore, E. M. et al. A recurrent mutation in the BMP type I receptor ACVR1 causes inherited and sporadic fibrodysplasia ossificans progressiva. *Nat. Genet.* **38**, 525–527 (2006).
22. Wallace, D. F. et al. A critical role for murine transferrin receptor 2 in erythropoiesis during iron restriction. *Br. J. Haematol.* **168**, 891–901 (2015).
23. Nai, A. et al. The erythroid function of transferrin receptor 2 revealed by Tmprss6 inactivation in different models of transferrin receptor 2 knockout mice. *Haematologica* **99**, 1016–1021 (2014).
24. Urist, M. R. Bone: formation by autoinduction. *Science* **150**, 893–899 (1965).
25. Roetto, A. et al. Comparison of 3 Tfr2-deficient murine models suggests distinct functions for Tfr2-alpha and Tfr2-beta isoforms in different tissues. *Blood* **115**, 3382–3389 (2010).
26. Herrmann, T. et al. Iron overload in adult Hfe-deficient mice independent of changes in the steady-state expression of the duodenal iron transporters DMT1 and Ireg1/ferroportin. *J. Mol. Med.* **82**, 39–48 (2004).
27. Altamura, S. et al. Resistance of ferroportin to hepcidin binding causes exocrine pancreatic failure and fatal iron overload. *Cell. Metab.* **20**, 359–367 (2014).
28. Tsay, J. et al. Bone loss caused by iron overload in a murine model: importance of oxidative stress. *Blood* **116**, 2582–2589 (2010).
29. Rishi, G., Secondes, E. S., Wallace, D. F. & Subramaniam, V. N. Normal systemic iron homeostasis in mice with macrophage-specific deletion of transferrin receptor 2. *Am. J. Physiol. Gastrointest. Liver Physiol.* **310**, G171–G180 (2016).
30. Kamiya, N. et al. Wnt inhibitors Dkk1 and Sost are downstream targets of BMP signaling through the type IA receptor (BMPRIA) in osteoblasts. *J. Bone Miner. Res.* **25**, 200–210 (2010).
31. Simsek Kiper, P. O. et al. Cortical-bone fragility–insights from sFRP4 deficiency in Pyle's disease. *N. Engl. J. Med.* **374**, 2553–2562 (2016).
32. Wosczyna, M. N., Biswas, A. A., Cogswell, C. A. & Goldhamer, D. J. Multipotent progenitors resident in the skeletal muscle interstitium exhibit robust BMP-dependent osteogenic activity and mediate heterotopic ossification. *J. Bone Miner. Res.* **27**, 1004–1017 (2012).
33. Shimono, K. et al. Potent inhibition of heterotopic ossification by nuclear retinoic acid receptor-gamma agonists. *Nat. Med.* **17**, 454–460 (2011).
34. Fransen, M. et al. Safety and efficacy of routine postoperative ibuprofen for pain and disability related to ectopic bone formation after hip replacement surgery (HIPAID): randomised controlled trial. *BMJ* **333**, 519 (2006).
35. Shen, G. S. et al. Hepcidin1 knockout mice display defects in bone microarchitecture and changes of bone formation markers. *Calcif. Tissue Int.* **94**, 632–639 (2014).
36. Guggenbuhl, P. et al. Bone status in a mouse model of genetic hemochromatosis. *Osteoporos. Int.* **22**, 2313–2319 (2011).
37. Doyard, M. et al. Decreased bone formation explains osteoporosis in a genetic mouse model of hemochromatosiss. *PLoS ONE* **11**, e0148292 (2016).
38. Calzolari, A. et al. TfR2 localizes in lipid raft domains and is released in exosomes to activate signal transduction along the MAPK pathway. *J. Cell. Sci.* **119**, 4486–4498 (2006).
39. Keller, S., Nickel, J., Zhang, J. L., Sebald, W. & Mueller, T. D. Molecular recognition of BMP-2 and BMP receptor IA. *Nat. Struct. Mol. Biol.* **11**, 481–488 (2004).
40. Yin, H., Yeh, L. C., Hinck, A. P. & Lee, J. C. Characterization of ligand-binding properties of the human BMP type II receptor extracellular domain. *J. Mol. Biol.* **378**, 191–203 (2008).
41. Canali, S., Wang, C. Y., Zumbrennen-Bullough, K. B., Bayer, A. & Babitt, J. L. Bone morphogenetic protein 2 controls iron homeostasis in mice independent of Bmp6. *Am. J. Hematol.* **92**, 1204–1213 (2017).
42. Koch, P. S. et al. Angiocrine Bmp2 signaling in murine liver controls normal iron homeostasis. *Blood* **129**, 415–419 (2017).
43. Ramos, E. et al. Evidence for distinct pathways of hepcidin regulation by acute and chronic iron loading in mice. *Hepatology* **53**, 1333–1341 (2011).
44. Li, X. et al. Targeted deletion of the sclerostin gene in mice results in increased bone formation and bone strength. *J. Bone Miner. Res.* **23**, 860–869 (2008).
45. MacDonald, B. T. et al. Bone mass is inversely proportional to Dkk1 levels in mice. *Bone* **41**, 331–339 (2007).
46. van Bezooijen, R. L. et al. Sclerostin is an osteocyte-expressed negative regulator of bone formation, but not a classical BMP antagonist. *J. Exp. Med.* **199**, 805–814 (2004).
47. Kamiya, N. et al. BMP signaling negatively regulates bone mass through sclerostin by inhibiting the canonical Wnt pathway. *Development* **135**, 3801–3811 (2008).
48. Yu, C. et al. Advanced oxidation protein products induce apoptosis, and upregulate sclerostin and RANKL expression, in osteocytic MLO-Y4 cells via JNK/p38 MAPK activation. *Mol. Med. Rep.* **15**, 543–550 (2017).
49. Croons, V., Martinet, W., Herman, A. G., Timmermans, J. P. & De Meyer, G. R. The protein synthesis inhibitor anisomycin induces macrophage apoptosis in rabbit atherosclerotic plaques through p38 mitogen-activated protein kinase. *J. Pharmacol. Exp. Ther.* **329**, 856–864 (2009).
50. Kamiya, N., Kaartinen, V. M. & Mishina, Y. Loss-of-function of ACVR1 in osteoblasts increases bone mass and activates canonical Wnt signaling through suppression of Wnt inhibitors SOST and DKK1. *Biochem. Biophys. Res. Commun.* **414**, 326–330 (2011).
51. Biswas, S. et al. BMPRIA is required for osteogenic differentiation and RANKL expression in adult bone marrow mesenchymal stromal cells. *Sci. Rep.* **8**, 8475 (2018).
52. Witcher, P. C. et al. Sclerostin neutralization unleashes the osteoanabolic effects of Dkk1 inhibition. *JCI Insight* **3**, e98673 (2018).
53. Lowery, J. W. et al. Loss of BMPR2 leads to high bone mass due to increased osteoblast activity. *J. Cell Sci.* **128**, 1308–1315 (2015).
54. Bao, Q. et al. Disruption of bone morphogenetic protein type IA receptor in osteoblasts impairs bone quality and bone strength in mice. *Cell Tissue Res.* **374**, 263–273 (2018).
55. Zhang, Y. et al. Loss of BMP signaling through BMPR1A in osteoblasts leads to greater collagen cross-link maturation and material-level mechanical properties in mouse femoral trabecular compartments. *Bone* **88**, 74–84 (2016).
56. Forsberg, J. A. et al. Heterotopic ossification in high-energy wartime extremity injuries: prevalence and risk factors. *J. Bone Jt. Surg. Am.* **91**, 1084–1091 (2009).
57. Regis, D., Sandri, A. & Sambugaro, E. Incidence of heterotopic ossification after surface and conventional total hip arthroplasty: a comparative study using anterolateral approach and indomethacin prophylaxis. *Biomed. Res. Int.* **2013**, 293528 (2013).
58. Chakkalakal, S. A. et al. Palovarotene inhibits heterotopic ossification and maintains limb mobility and growth in mice with the human ACVR1(R206H) fibrodysplasia ossificans progressiva (FOP) mutation. *J. Bone Miner. Res.* **31**, 1666–1675 (2016).
59. Agarwal, S. et al. mTOR inhibition and BMP signaling act synergistically to reduce muscle fibrosis and improve myofiber regeneration. *JCI Insight* **1**, e89805 (2016).
60. Hino, K. et al. Activin-A enhances mTOR signaling to promote aberrant chondrogenesis in fibrodysplasia ossificans progressiva. *J. Clin. Invest.* **127**, 3339–3352 (2017).
61. Rodda, S. J. & McMahon, A. P. Distinct roles for Hedgehog and canonical Wnt signaling in specification, differentiation and maintenance of osteoblast progenitors. *Development* **133**, 3231–3244 (2006).
62. Nakamura, T. et al. Estrogen prevents bone loss via estrogen receptor alpha and induction of Fas ligand in osteoclasts. *Cell* **130**, 811–823 (2007).
63. Clausen, B. E., Burkhardt, C., Reith, W., Renkawitz, R. & Forster, I. Conditional gene targeting in macrophages and granulocytes using LysMcre mice. *Transgenic Res.* **8**, 265–277 (1999).
64. Rhee, Y. et al. PTH receptor signaling in osteocytes governs periosteal bone formation and intracortical remodeling. *J. Bone Miner. Res.* **26**, 1035–1046 (2011).
65. Liu, X. et al. A novel mouse model of trauma induced heterotopic ossification. *J. Orthop. Res.* **32**, 183–188 (2014).
66. Norden, D. M. et al. Ibuprofen ameliorates fatigue- and depressive-like behavior in tumor-bearing mice. *Life Sci.* **143**, 65–70 (2015).

67. Bassett, J. H. et al. Optimal bone strength and mineralization requires the type 2 iodothyronine deiodinase in osteoblasts. *Proc. Natl. Acad. Sci. USA* **107**, 7604–7609 (2010).
68. Rauner, M. et al. Increased EPO levels are associated with bone loss in mice lacking PHD2 in EPO-producing cells. *J. Bone Miner. Res.* **31**, 1877–1887 (2016).
69. Theurl, I. et al. On-demand erythrocyte disposal and iron recycling requires transient macrophages in the liver. *Nat. Med.* **22**, 945–951 (2016).
70. Liberzon, A. et al. The Molecular Signatures Database hallmark gene set collection. *Cell Syst.* **1**, 417–425 (2015).
71. Park, K. W. et al. The small molecule phenamil induces osteoblast differentiation and mineralization. *Mol. Cell. Biol.* **29**, 3905–3914 (2009).
72. Liberzon, A. et al. Molecular signatures database (MSigDB) 3.0. *Bioinformatics* **27**, 1739–1740 (2011).

Acknowledgements

We would like to thank our technicians for their excellent work. We thank the Core Facility Cellular Imaging of TU Dresden for their support with the confocal microscope and the acquisition of immunofluorescence images and A. Drescher and J. Nickel for critical suggestions regarding SPR analyses. This work was supported by the German Research Foundation (DFG-SFB655 to L.C.H. and U.P.; TRR-67 to V.H. and L.C.H.; µBONE to M.R. and L.C.H.; RA1923/12-1 to M.R.) and MedDrive start-up grants from the Medical Faculty of the Technische Universität Dresden (M.R. and U.B.). M.R. was supported by the Support-the-Best Initiative of the TUD funded through the Excellence initiative of the German Federal and State Governments. J.H.D.B. and G.R.W. received a Wellcome Trust Joint Investigator Award (110141/Z/15/Z and 110140/Z/15/Z).

Author contributions

M.R., U.B., A.R., J.S-H., S.R., U.P., and L.C.H. designed experiments. M.R., U.B., A.R., R.M.P., J.S.-H., H.W., S.R., G.C., A.P., R.L., I.H., S.C., and D.K.E. performed experiments and analysed data. T.B., S.A., S.C., M.U.M., and I.T. provided mouse bone samples. M.R., U.B., A.R., J.S.-H., H.W., S.R., V.H., I.H., T.B., M.U.M., J.H.D.B., G.R.W., G.S., I.T., U.P., and L.C.H. interpreted the data and provided critical comments on the manuscript. M.R., U.B., and L.C.H. wrote the manuscript. All authors provided critical review of the manuscript.

Competing interests

The Technische Universität Dresden holds a patent for the use of Tfr2-ECD to treat heterotopic ossification and other related bone excess diseases (PCT/EP2018/065846). Moreover, a patent application has been filed at the European Patent Office for the use of Tfr2 blockade for the treatment of bone and haematological diseases (#18 177 441.5, 19.06.2018). M.R., U.B., U.P., and L.C.H. are the inventors of both patents. I.T. is a consultant for Kymab Ltd. The other authors declare no competing interests.

Additional information

Supplementary information is available for this paper at https://doi.org/10.1038/s42255-018-0005-8.

Reprints and permissions information is available at www.nature.com/reprints.

Correspondence and requests for materials should be addressed to M.R.

Publisher's note: Springer Nature remains neutral with regard to jurisdictional claims in published maps and institutional affiliations.

© The Author(s), under exclusive licence to Springer Nature Limited 2019

nature research

Corresponding author(s): Martina Rauner, PhD

☐ Initial submission ☐ Revised version ☒ Final submission

Life Sciences Reporting Summary

Nature Research wishes to improve the reproducibility of the work that we publish. This form is intended for publication with all accepted life science papers and provides structure for consistency and transparency in reporting. Every life science submission will use this form; some list items might not apply to an individual manuscript, but all fields must be completed for clarity.

For further information on the points included in this form, see Reporting Life Sciences Research. For further information on Nature Research policies, including our data availability policy, see Authors & Referees and the Editorial Policy Checklist.

Experimental design

1. Sample size

   Describe how sample size was determined.

   Sample sizes were chosen based on experience from previous studies to balance the ability to measure significant differences while reducing the number of animals used. Sample sizes were adjusted in some rodent studies when greater biological variability was expected due to use of a mixed background strain.
   For gene and protein expression level analysis by qPCR and Western Blot as well as ELISA, combining a technical duplicate (intra-sample variability) with at least a biological triplicate (inter-experiment variability) was applied to detect a pre-specified effect size.

2. Data exclusions

   Describe any data exclusions.

   No data were excluded from successfully performed experiments.

3. Replication

   Describe whether the experimental findings were reliably reproduced.

   All attempts at replication were successful. Key experiments were performed at least two independent times and were replicated by two different investigators. For some findings, several methods have been used to verify the results.

4. Randomization

   Describe how samples/organisms/participants were allocated into experimental groups.

   The animals were randomly assigned to experimental groups.

5. Blinding

   Describe whether the investigators were blinded to group allocation during data collection and/or analysis.

   Investigators were not blinded for group allocation for practical reasons. However, during data collection and analyses, the experimentors were blinded.

Note: all studies involving animals and/or human research participants must disclose whether blinding and randomization were used.

6. Statistical parameters

For all figures and tables that use statistical methods, confirm that the following items are present in relevant figure legends (or in the Methods section if additional space is needed).

n/a	Confirmed
☐	☒ The exact sample size (*n*) for each experimental group/condition, given as a discrete number and unit of measurement (animals, litters, cultures, etc.)
☐	☒ A description of how samples were collected, noting whether measurements were taken from distinct samples or whether the same sample was measured repeatedly
☐	☒ A statement indicating how many times each experiment was replicated
☐	☒ The statistical test(s) used and whether they are one- or two-sided (note: only common tests should be described solely by name; more complex techniques should be described in the Methods section)
☐	☒ A description of any assumptions or corrections, such as an adjustment for multiple comparisons
☐	☒ The test results (e.g. *P* values) given as exact values whenever possible and with confidence intervals noted
☐	☒ A clear description of statistics including central tendency (e.g. median, mean) and variation (e.g. standard deviation, interquartile range)
☐	☒ Clearly defined error bars

See the web collection on statistics for biologists for further resources and guidance.

Software

Policy information about availability of computer code

7. Software

Describe the software used to analyze the data in this study.	Microsoft Office Excel and Graphpad Prism 6.0 were used to perform statistical analyses. Gene ontology analyses of next generation sequencing were performed with Cytoscape 3.2.1 and the ClueGO plugin.

For manuscripts utilizing custom algorithms or software that are central to the paper but not yet described in the published literature, software must be made available to editors and reviewers upon request. We strongly encourage code deposition in a community repository (e.g. GitHub). *Nature Methods* guidance for providing algorithms and software for publication provides further information on this topic.

Materials and reagents

Policy information about availability of materials

8. Materials availability

Indicate whether there are restrictions on availability of unique materials or if these materials are only available for distribution by a for-profit company.	All materials in this study are either available from authors or from companies listed in Method section.

9. Antibodies

Describe the antibodies used and how they were validated for use in the system under study (i.e. assay and species).

The following primary antibodies were used for western blot and immunhistological staining:
ß-actin (rabbit): Cell Signaling, cat# 4970, clone 13E5, dilution 1:2000
Axin-2 (rabbit): Abcam, cat#ab107613, dilution 1:500
ß-catenin (rabbit) for WB: Cell Signaling, cat# 9582, clone 6B3, dilution 1:1000
ß-catenin for IHC (rabbit): Sigma-Aldrich, cat# C2206, dilution 1:2000
ß-tubulin (rabbit): Cell Signaling, cat#2146, dilution 1:1000
Connexin-43 (rabbit): Cell Signaling, #3512, dilution 1:1000
Erk (p44/42 MAPKinase) (rabbit): Cell Signaling, cat# 4695, clone 137F5, dilution 1:1000
GAPDH (rabbit): Hytest, cat#5G4, dilution 1:1000
Lamin A/C (rabbit): Santa Cruz, cat# sc-20681; dilution 1:1000
Osterix (mouse): Santa Cruz, cat# sc-393325; dilution 1:500
phospho-Erk (rabbit): Cell Signaling, cat# 4370, clone D13.14.4E, dilution 1:1000
p38 (rabbit): Cell Signaling, cat# 9212,dilution: 1:1000
phospho-p38 (rabbit): Cell Signaling, cat# 4511, clone D3F9, dilution 1:500
phospho-Smad1/5 (rabbit): Cell Signaling, cat# 9516, clone 13E5, dilution 1:1000
phospho-Smad 1/5/8 (rabbit): Cell Signaling, cat# 13820P; clone D5B10, dilution 1:1000
Smad5 (rabbit): Cell Signaling, cat# 9517, dilution 1:1000
Tfr2 (H-140) (rabbit): Santa Cruz, cat# sc-48747, dilution 1:1000
HA (HA-7)(mouse): Sigma Aldrich, cat# H9658, dilution 1:1000
FLAG (rabbit): Sigma Aldrich, cat# F7425, dilution 1:1000

Secondary antibodies for WB
anti-rabbit IgG, Cell Signaling, cat# 7074, dilution 1:2000
anti-mouse IgG, Sigma Aldrich, cat# A9044, dilution 1:5000
Secondary antibodies for IHC
Alexa Fluor 594 F(ab) 2 fragment goat anti-rabbit IgG (H+L), Invitrogen, cat# A11072, dilution 1:1000

10. Eukaryotic cell lines

a. State the source of each eukaryotic cell line used.

Huh-7 Human Hepatoma cell line

b. Describe the method of cell line authentication used.

Gene expression response of hepatic genes upon specific stimuli

c. Report whether the cell lines were tested for mycoplasma contamination.

Mycoplasma test was negative

d. If any of the cell lines used are listed in the database of commonly misidentified cell lines maintained by ICLAC, provide a scientific rationale for their use.

No commonly misidentified cell lines were used.

Animals and human research participants

Policy information about studies involving animals; when reporting animal research, follow the ARRIVE guidelines

11. Description of research animals

Provide details on animals and/or animal-derived materials used in the study.

Tfr2-/- mice were on a 129/sv background. Tfr2fl/fl; CtskCre, Tfr2fl/fl; OsxCre mice, Tfr2fl/fl; LysmCre mice as well as Tfr2-/-; Dmp1-SOST-tg mice were on a mixed sv129/C57BL/6 background. Male and female mice were used at 10 -12 weeks of age. For some experiments, older mice aged 6 -12 months were used.

Policy information about studies involving human research participants

12. Description of human research participants

Describe the covariate-relevant population characteristics of the human research participants.

No human data were used in this study.